


ORIGINAL ARTICLE

Open Access



Retrospect and prospect of ionospheric weather observed by FORMOSAT-3/COSMIC and FORMOSAT-7/COSMIC-2

Tiger Jann-Yenq Liu^{1,2,3*} , Charles Chien-Hung Lin⁴, Chi-Yen Lin^{1,2}, I-Te Lee⁵, Yang-Yi Sun⁶, Shih-Ping Chen⁴, Fu-Yuan Chang², Panthalingal Krishnanunni Rajesh⁴, Chih-Ting Hsu⁷, Tomoko Matsuo⁸, Chia-Hung Chen⁴ and Ho-Fang Tsai⁴

Abstract

FORMOSAT-3/COSMIC (F3/C) constellation of six micro-satellites was launched into the circular low-earth orbit at 800 km altitude with a 72-degree inclination angle on 15 April 2006, uniformly monitoring the ionosphere by the GPS (Global Positioning System) Radio Occultation (RO). Each F3/C satellite is equipped with a TIP (Tiny Ionospheric Photometer) observing 135.6 nm emissions and a TBB (Tri-Band Beacon) for conducting ionospheric tomography. More than 2000 RO profiles per day for the first time allows us globally studying three-dimensional ionospheric electron density structures and formation mechanisms of the equatorial ionization anomaly, middle-latitude trough, Weddell/Okhotsk Sea anomaly, etc. In addition, several new findings, such as plasma caves, plasma depletion bays, etc., have been reported. F3/C electron density profiles together with ground-based GPS total electron contents can be used to monitor, nowcast, and forecast ionospheric space weather. The S4 index of GPS signal scintillations recorded by F3/C is useful for ionospheric irregularities monitoring as well as for positioning, navigation, and communication applications. F3/C was officially decommissioned on 1 May 2020 and replaced by FORMOSAT-7/COSMIC-2 (F7/C2). F7/C2 constellation of six small satellites was launched into the circular low-Earth orbit at 550 km altitude with a 24-degree inclination angle on 25 June 2019. F7/C2 carries an advanced TGRS (Tri Gns (global navigation satellite system) Radio occultation System) instrument, which tracks more than 4000 RO profiles per day. Each F7/C2 satellite also has a RFB (Radio Reference Beacon) on board for ionospheric tomography and an IVM (Ion Velocity Meter) for measuring ion temperature, velocity, and density. F7/C2 TGRS, IVM, and RFB shall continue to expand the F3/C success in the ionospheric space weather forecasting.

Key Points

- FORMOSAT-3/COSMIC and FORMOSAT-7/COSMIC-2 uniformly observe 3D electron density.
- FORMOSAT-3 and FORMOSAT-7 enable ionospheric weather forecasting.
- FORMOSAT-7/COSMIC-2 TGRS and IVM have a better understanding of the electrodynamics of ionospheric plasma.

*Correspondence: jyliu@jupiter.ss.ncu.edu.tw

¹ Center for Astronautical Physics and Engineering, National Central University, Taoyuan City, Taiwan
Full list of author information is available at the end of the article

Keywords: Ionospheric weather, FORMOSAT-3/COSMIC, FORMOSAT-7/COSMIC-2, Radio occultation, GNSS

1 Introduction

The part of the atmosphere above about 60 km altitude, where free electrons exist in numbers sufficient to influence the travel of radio waves, is termed the ionosphere. People heavily rely on the modern technologies of satellite positioning, navigation and telecommunication, which can be significantly affected by ionospheric weather conditions from space, Earth's atmosphere, and lithosphere (Ratcliffe 1972; Davies 1990; Kelley 2009). In Taiwan, research and education of ionospheric physics began with a ground-based ionosonde operated by the Ministry of Communications in 1952 and courses of ionospheric physics offered by National Central University in 1959, respectively. The development of ionospheric sciences has been much faster since 1999, after National Space Organization (NSPO) of Taiwan started launching a series of FORMOSAT satellites (Liu et al. 2016a). A major turning point in the field of atmospheric and ionospheric research was the launch of FORMOSAT-3/COSMIC (Constellation Observing System for Meteorology, Ionosphere and Climate) on 15 April 2006 (Cheng et al. 2006). The mission was part of a collaborative program between NSPO and The University Corporation for Atmospheric Research (UCAR) of the United States (US) to collect atmospheric data for weather prediction, and for ionosphere and climate research. Six FORMOSAT-3/COSMIC (F3/C) micro-satellites travel on circular low-earth orbit at 800 km altitude with 72-deg inclination, observing the atmosphere and ionosphere continuously. The primary payload of F3/C is the GPS (Global Positioning System) Occultation Experiment (GOX), which receives the radio wave signals transmitted from the GPS satellites. Based on the time delay and the bending angle of GPS signals recorded by the radio occultation (RO) technique, the electron density profiles in the ionosphere as well as temperature, pressure, and water content profiles in the atmosphere can be derived (Anthes et al. 2008). There are also two other payloads carried by each F3/C satellite including, a tiny ionospheric photometer (TIP) to observe the nighttime ionospheric airglow emission of 135.6 nm emissions around the F2-peak height (Chua et al. 2009; Coker et al. 2009; Dymond et al. 2009), and a tri-band beacon (TBB) to tomographically estimate fine structures of ionospheric electron density and scintillations of the signals on the satellite-to-receiver plane (Hsiao et al. 2009).

More than 2000 RO profiles per day allow scientists for the first time globally and uniformly examining ionospheric electron density profiles, observing

three-dimensional (3D) structures of the equatorial ionization anomaly (Lin et al. 2007a), middle-latitude trough (Lee et al. 2011), Weddell/Okhotsk Sea anomaly (Lin et al. 2009, 2010; Chang et al. 2015), etc.; finding several new features of plasma caves (Liu et al. 2010a), midlatitude electron density enhancement (Rajesh et al. 2016), plasma depletion bays (Chang et al. 2020), etc.; observing ionospheric signatures induced by seismic/tsunami waves (Sun et al. 2016; Liu et al. 2019), earthquake precursors (Liu et al. 2009), etc. and developing monitoring (Sun et al. 2017), nowcast (Lin et al. 2015, 2017), forecast (Lee et al. 2012a; Hsu et al. 2014; Chen et al. 2016a) models for ionospheric space weather. The above three models developed by National Central University and National Cheng Kung University have been adopted by Space Weather Operational Office at Central Weather Bureau for the routine operation of ionospheric space forecast. Moreover, scintillations of GPS signals in the S4 index recorded by F3/C are used to study ionospheric plasma irregularities and construct models for positioning, navigation, and communication applications (Liu et al. 2016b; Chen et al. 2017b). The global and uniform 3D electron density RO observations of F3/C have the ionospheric weather forecast being possible.

Following the success of the F3/C program, NSPO and the National Oceanic and Atmospheric Administration (NOAA) of the US launched FORMOSAT-7/COSMIC-2 (F7/C2) satellites on June 25, 2019 (Chu et al. 2021). F7/C2 constellation consists of six small satellites at an altitude of 550 km, with an inclination angle of 24 degrees, and orbiting period of about 97 min. Each F7/C2 satellite is equipped with a RO receiver, the Tri GNSS (Global Navigation Satellite System) Radio occultation System (TGRS), which receives the refracted signals from the GNSS satellites. The F7/C2 constellation observes about 4000 electron density profiles per day between 45 degrees north and south latitudes for space weather monitoring. In addition to TGRS, the Ion Velocity Meter (IVM) measures the temperature, velocity, and density of ions, and the RF Beacon (RFB) is used to conduct the 3D ionospheric tomography. Liu (2019) presented the first F7/C2 ionospheric RO observations in the 20th International Beacon Satellite Symposium, while Liu et al. (2020a, 2020b) report ionospheric earthquake precursors and space weather observed by F7/C2 during American Geophysical Union Fall Meeting 2020. Lin et al. (2020b) validate F7/C2 space weather products of Global Ionospheric Specification (GIS) and Ne-Aided Abel electron density profile. Rajesh et al. (2021) examine an unexpected and

extreme positive ionospheric response to a minor magnetic storm on August 5, 2019, by using GIS 3D electron density profiles obtained by assimilating radio occultation total electron content (TEC) measurements of the F7/C2 satellites, and ground-based GNSS TEC. Chen et al. (2021a) study the ionospheric scintillation in the F layer using the S4 index derived from F7/C2 RO observations and conduct near real-time global plasma irregularity monitoring. Concurrent F7/C2 RO and IVM observations enable a better understanding of the electrodynamics of plasma in the low-latitude ionosphere.

2 F3/C ionospheric observations and new findings

This section overviews the F3/C ionospheric RO observations on conspicuous features of the equatorial ionization anomaly (EIA) in equatorial/low latitudes, middle-latitude trough, and Weddell Sea Anomaly/Okhotsk Sea Anomaly (WSA/OSA) in middle/high latitudes, as well as new findings of the plasma caves and plasma depletion bays (PDBs) in equatorial/low latitudes. The EIA crests yield the greatest electron density of the globe, while the middle latitude trough has the smallest one. Furthermore, the electron density over the WAS/OSA areas during nighttime is oppositely greater than those during daytime in the summer hemisphere. In addition to the feature of non-migrating tides of wave-number 4 (WN4) in equatorial/low latitude ionosphere, new findings of plasma caves and PDBs as well as their signs of progress are summarized.

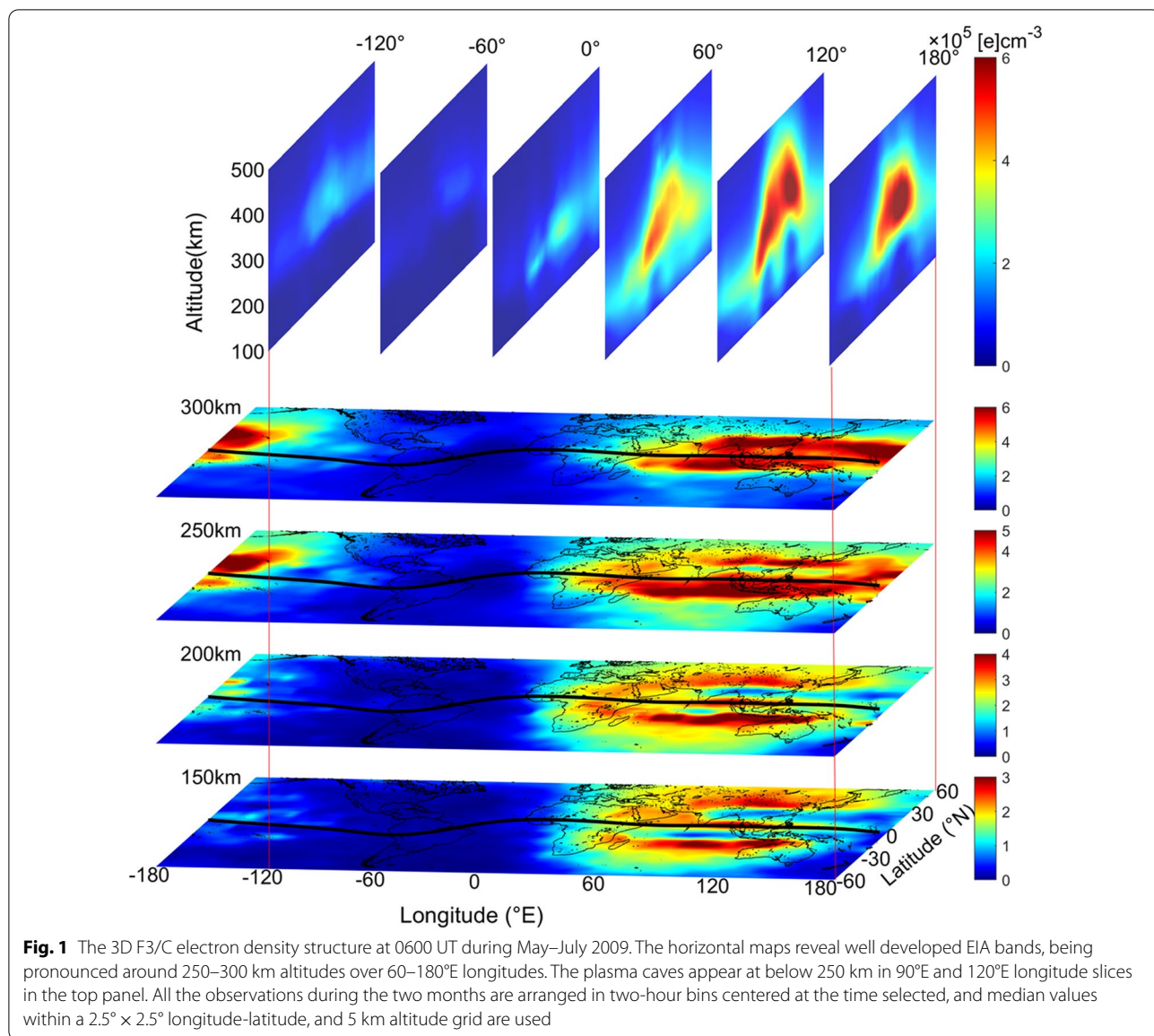
2.1 Equatorial ionization anomaly

Despite being one of the most prominent features of the low-latitude ionosphere that continues to attract the attention of the ionospheric community, it was not until the launch of the F3/C mission that the 3D global maps of EIA based on actual measurements became available to the community. Lin et al. (2007a) successfully combined multiple days of RO profiles to generate latitude-altitude maps of electron density, depicting the time evolution of EIA, which was otherwise portrayed mainly in textbook sketches or by using model simulations. They offered an observation-based visualization to the existing perception of EIA (Appleton and Naismith 1935), which they describe as “two enhanced plasma crests at low latitudes straddling the magnetic equator, yielding the greatest electron density in the globe, with depleted electron density over the magnetic equator”. They further demonstrated the potential of this unique space-based soundings of the F3/C cluster by illustrating the time evolution of the ionization crests on both sides of the magnetic equator; conveying the physics of the well-known equatorial plasma fountain to the enthusiastic students and

researchers much clearer than any textbook description would do.

Figure 1, a snapshot of the global electron density distribution at 0600 UT by combining the measurements during May–July 2009, illustrates how the F3/C ionospheric RO profiles allow scientists to observe the 3D EIA structures globally and uniformly, adopting the demonstration used by Lin et al. (2009). In these three months, the Northern and Southern Hemispheres are in the summer and winter seasons, respectively. At the low latitude region over the sunlit longitudes, both the vertical and horizontal slices depict the two EIA bands of dense electron density straddling the magnetic equator. The EIA bands tend to be farther from the magnetic equator at lower altitudes compared to higher altitudes during daytime. The figure depicts well established characteristic features of the low-latitude electron density, while also revealing new aspects that elicited additional validation experiments. For example, examining the horizontal slice at 250 km altitude, the southern EIA band is seen closer to the magnetic equator than the northern one, portraying the characteristic role of neutral wind in modifying the EIA density and location in solstice months. The near-midday vertical electron density profiles at the top between 90°E and 120°E longitudes, on the other hand, show a previously unknown cave or tunnel like feature in the latitude distribution, aptly named as plasma cave or tunnel, appearing prominently below 250 km altitude.

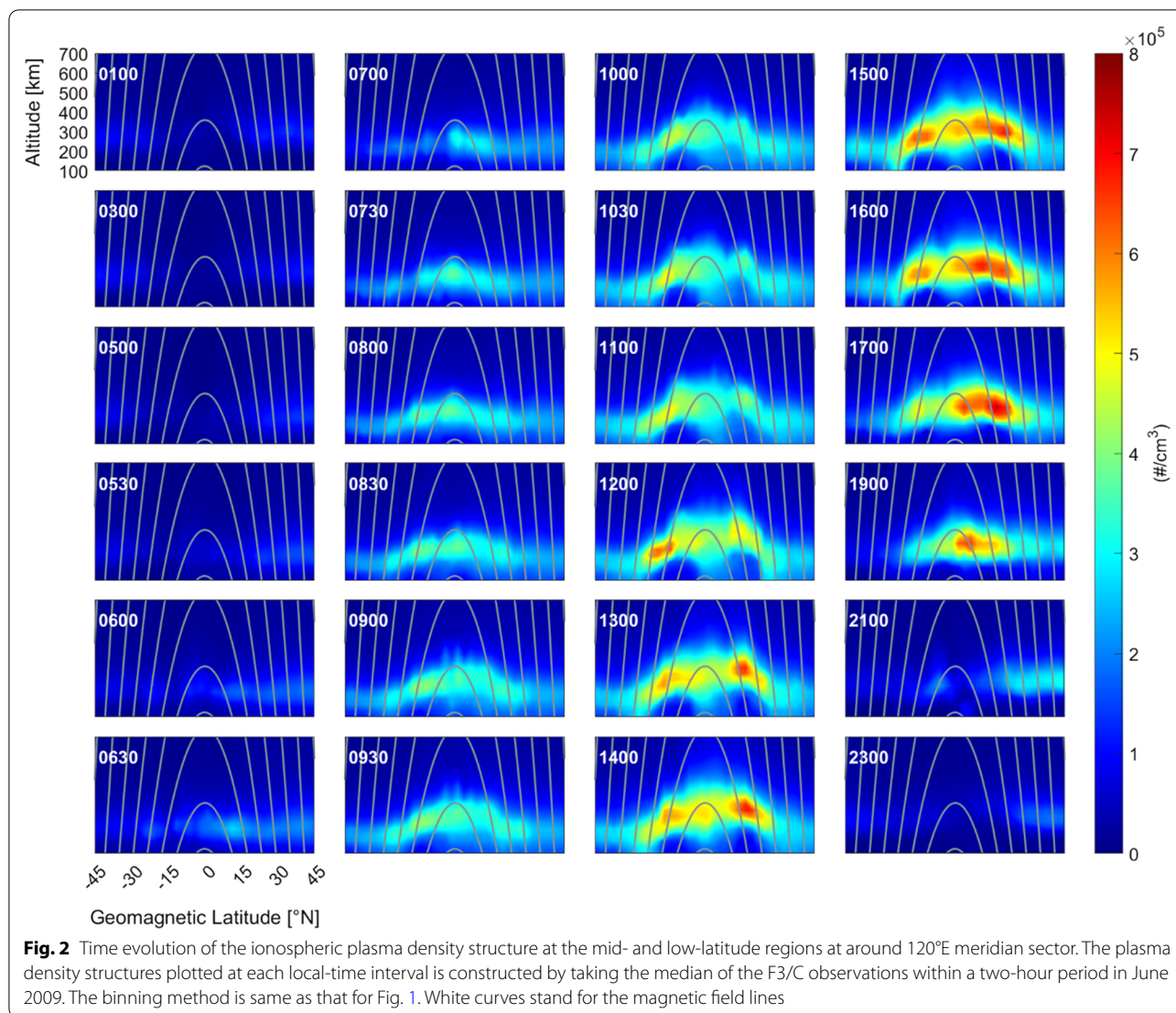
Without delving into the details, how such global electron density maps help to exemplify the conceptual understanding of the evaluation of daytime low-latitude ionosphere is examined first. Figure 2 displays the time sequence of development and decay of the EIA crests over 120°E meridian plane (i.e., Taiwan longitude) during a 24-h period in June 2009, adopting the analysis methodology and illustration used by Lin et al. (2007a), revealing mostly similar overall features as in their results. The figure offers an observational illustration to the theoretical understanding of EIA formation by $E \times B$ force lifting plasma to higher altitudes perpendicular to the magnetic field-lines over the equatorial latitudes and forming the EIA crests as the plasma diffuses down along magnetic field lines and accumulates at low-latitudes (cf. Rishbeth 2000). In addition, the figure visualizes the impact of neutral wind in influencing the strength and location of the EIA crests, leading to seasonal or winter anomaly (Torr and Torr 1973; Torr et al. 1980). The electron density in the northern hemisphere starts to strengthen first owing to the earlier sunrise time, and the southern EIA crest becomes stronger during 0800–1200 LT as a result of summer-to-winter hemisphere plasma transport and the asymmetric neutral composition distribution before noon. Subsequently, the northern EIA crest



becomes stronger and maximizes at about 1600 LT and disappears after 1900 LT as the plasma fountain weakens and the production shuts down. More discussion of such dynamic interactions in the asymmetric development of the EIA crests as imaged by the F3/C can be found in the works of Lin et al. (2007a), and Tulası Ram et al. (2009).

As demonstrated above, such a representation of the time-dependent images of the ionospheric electron density by accumulating the observations taken over a selected period provides unprecedented details of the EIA structure and evolution. The impact of this fresh representation of the global 3D electron density structure (Figs. 1, 2) was so outstanding that several researchers adopted a similar approach to investigate various

morphological features of global electron density distribution. The plasma cave/tunnel feature mentioned earlier could be identified because of such a visualization of the low-latitude ionosphere possible by using the F3/C electron density profiles. After more than 70 years since the EIA feature was first reported, Liu et al. (2010a) find that underneath the two EIA crests, two dome-shaped plasma caves are seen in the vertical slices of 90°E and 120°E longitudes (Fig. 1). These two caves are also found as depleted bands in the horizontal slices at 150 and 200 km altitudes. They carried out RO observation simulation experiment and confirmed that this new observation of cave structures are artifacts of Abel inversion, appearing mainly below 250 km altitude when the EIA crests are



well developed. While offering a correction to mitigate such artificial structures, they noted that the RO technique could not conclusively detect or rule out such cave or tunnel structures.

Though regarded as possible artificial structures, the plasma caves revealed in the F3/C electron density maps led to additional independent observations/simulations about similar features. Lee et al. (2012a) report plasma cave structures in International Reference Ionosphere (IRI) empirical model simulation, and further confirm their existence at low altitudes in the situ measurements of ion and electron densities by DE-2 satellite. They attribute the cave formation to unusually strong relative upward ion drifts on either side of the equator at lower altitudes. Chen et al. (2014) utilized SAMI3 (Sami3 is Also a Model of the Ionosphere) to reproduce plasma cave structures. They proposed

that the latitudinal gradient of meridional neutral wind could result in plasma flux convergence over the equator and divergence at off-equatorial latitudes, thus producing plasma caves. Tidal-decomposition analysis further suggested that the migrating terdiurnal tidal component (TW3) of the neutral winds is responsible for the converging meridional wind patterns over the equator, thus yielding the cave structure. Since the model winds used in the simulations were forced only by diurnal and semi-diurnal tidal modes at the lower boundary, the TW3 component is possibly in situ modulated. Such investigations highlight the importance of the F3/C mission, and how these unique measurements paved the way for numerous new investigations by eliminating one of the major constraints of insufficient global coverage. The following sections make an attempt to provide a flavor of such new findings and

major achievements since the commissioning of the F3/C mission.

2.2 Plasma depletion bay

Similar to the detection of plasma caves, PDB is another peculiar ionospheric phenomenon reported first time by Chang et al. (2020) with the help of the 3D global electron density maps constructed by using the F3/C measurements. While examining the F3/C electron density profiles during 2007–2014, they identify a new kind of ionospheric feature, which they termed as PDB based on their resemblance to the ocean bay structure, prominently appearing during the nighttime in solstice months. They describe PDB as “a broad region of low-density plasma at low-latitudes, giving a visual appearance of low plasma density in the winter hemisphere extending to the summer hemisphere of generally high plasma density, as if ocean water finds its way to low-level lands forming ocean bays”. The manifestation of PDBs in the F3/C electron density maps is illustrated in Fig. 3, which shows the monthly variations of the electron density at 300 km altitude at 2300 LT in 2008. In the left panels, a region of depleted electron density could be seen “curving in” to the southern hemisphere from the northern hemisphere over Southwest America longitude of 75–135°W in during October–March. This is called north plasma depletion bay, or North PDB. The right panels reveal three similar features “curving in” to the northern hemisphere over North Atlantic (60°W to 30°E), Indian Ocean (45–110°E), and Southeast Asia (120–170°E) longitudes during April–September. They constitute the South PDBs.

It can be seen that the North PDB appears pronounced in January, whereas the South PDBs are prominent in the June–July months, indicating that the PDB feature is strongest when the “bay hemisphere” is in the winter season. Chang et al. (2020) notes that the PDBs appear pronounced over 275–300 km altitudes around 2300–0100 LT, and their strength is inversely related to solar activity. They suggest that summer-to-winter field-aligned neutral wind elevates plasma upward and equatorward, thus causing the depleted patches to form at lower altitudes in the summer hemisphere. The summer-to-winter neutral wind also produces an upwelling in the summer hemisphere and downwelling in the winter hemisphere. This would decrease $[O]/[N_2]$ in the summer hemisphere, further facilitating the plasma loss. As these trans-equatorial winds transport plasma in the winter hemisphere to further lower altitudes, they rapidly recombine to generate a bay like curving feature of low electron density region protruding into the winter hemisphere. Chang et al. (2020) also shows that PDB structures indeed exist in the 135.6 nm airglow intensity measured by TIMED/GUVI, compared with concurrent F3/C electron density.

However, they appear prominently in the F3/C global electron density maps, which made identifying such features easier.

2.3 Vertical coupling of lower atmosphere and ionosphere

It is indeed a remarkable coincidence that the F3/C mission was launched during a period that witnessed some of the most fascinating observations in the ionospheric research, (1) the longitudinal wave-4 pattern that modifies the EIA electron density distribution, and (2) unexpected ionospheric variations during sudden stratospheric warming (SSW) events; both phenomena being related to the coupling between lower atmosphere and ionosphere. This section mainly aims to briefly highlight the contributions in the study of these features by using F3/C observations.

The longitudinal wave-4 structure manifest as four enhanced equatorial plasma regions, revealed in space-based airglow images over EIA latitudes (Sagawa et al. 2005; Immel et al. 2006), overlapping with the longitudes of the E-region maxima of the diurnal eastward wave-3 (DE3) nonmigrating tide (e.g., Oberheide et al. 2003; Forbes et al. 2006) in a global fixed local-time frame. These incredible observations led to the hypothesis of the lower-atmospheric forcing from latent heat release of deep tropospheric convection impacting the electron density distribution at F-region altitudes by modifying the E-region dynamo electric field (Sagawa et al. 2005; England et al. 2006; Immel et al. 2006). Following the discovery of the vertical coupling, Lin et al. (2007b), effectively made use of the 3D electron density measurements by F3/C to report, for the first time, the vertical structure of the longitudinal modulation of EIA. The fact that the longitudinal wave-4 pattern was mostly limited to the F-region altitudes confirmed the suggestion of tidal wind modulation affecting the E-region dynamo rather than directly influencing the F-region electron density. They further show hemispheric asymmetry of the 4-peak structure, which also vary with longitude, indicating such asymmetries in tidal effects and wind pattern.

An illustration of the fixed local time electron density maps constructed by using F3/C RO measurements is given in Fig. 4, revealing the time evolution of the four peaked EIA structure at 450 km altitude during September 2008. The longitudinal modulation starts forming by 0900 LT, and appear pronounced during the noon/post-noon hours of 1300–1700 LT, weakens during 2100–2300 LT, and becomes indistinguishable in the pre-sunrise hours after 0100 LT. Such diurnal characteristics of the wave-4 pattern was first described by Lin et al. (2007c) using the early F3/C observations in September–October 2008, reporting more-or-less similar local time variation as seen in the figure. They find that this local time

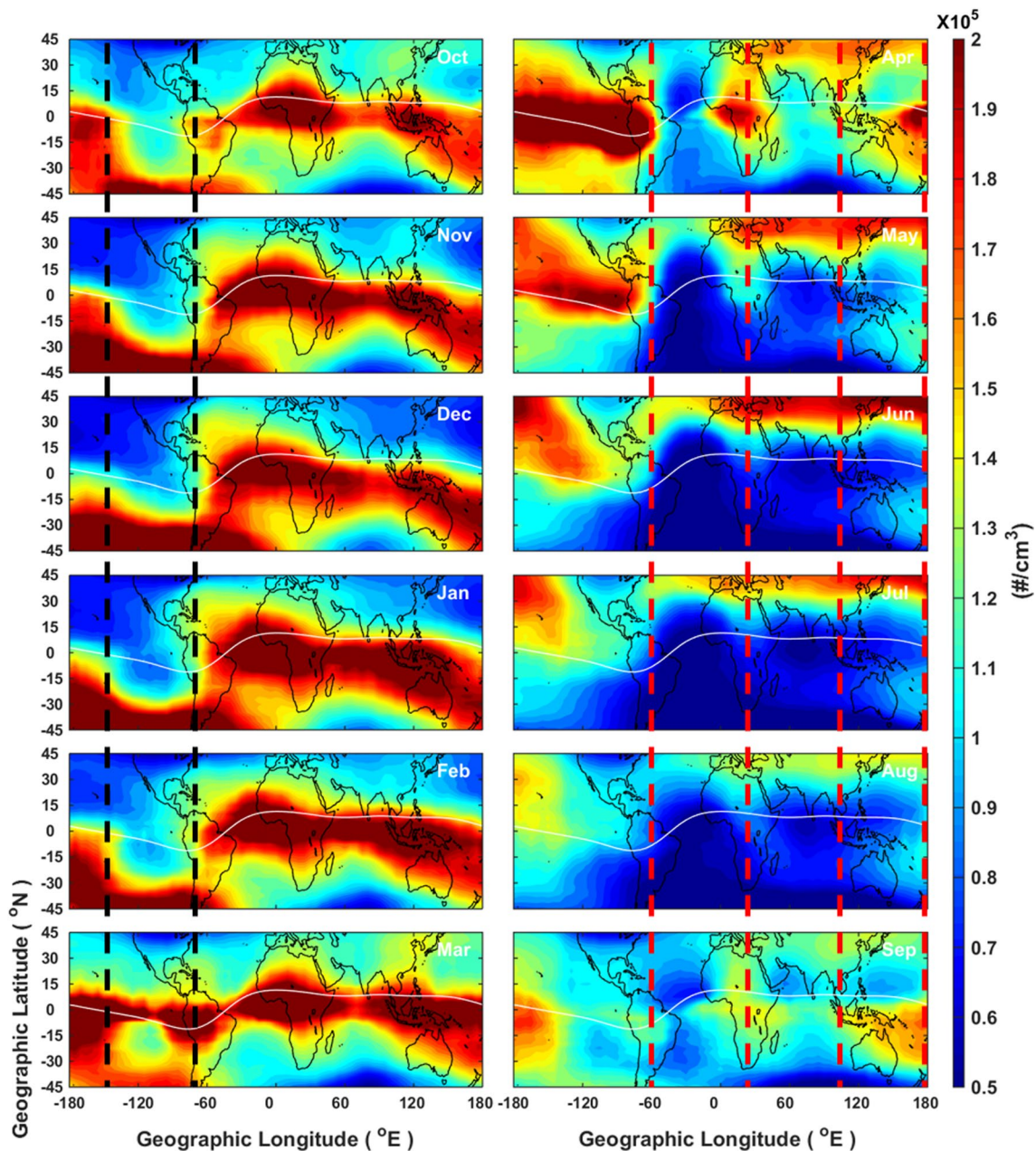


Fig. 3 Monthly plots of the F-3/C electron density at 300 km in the global constant local time maps at 2300 LT of 2008. Black and red dash lines indicate the longitudinal sectors of the one North PDB and the three South PDBs, respectively. The F3/C occultation observations are first subdivided into 12 months by binning about 60 days of data (i.e., from 15 days prior till 15 days after for each month) in every two-hour interval and median value of the soundings within each $5^\circ \times 2.5^\circ$ (longitude-latitude) grid at 25 km altitude levels is used

variation is consistent with the diurnal variation of the vertical $E \times B$ drift from the empirical model of Scherliess and Fejer (1999). They further confirm the hypothesis of DE3 nonmigrating tide modulating the equatorial plasma fountain and yielding the four-peaked pattern by comparing the latitude expansion of the EIA crests over the longitudes of stronger and weaker EIA, while also noting

that the eastward propagation of the wave-4 peak locations is slower than the phase velocity of DE3.

Following such earlier attempts to examine the longitudinal wave-4 pattern, the global F3/C RO measurements were soon recognized as a very valuable dataset in examining the migrating and non-migrating components of ionospheric oscillations by performing

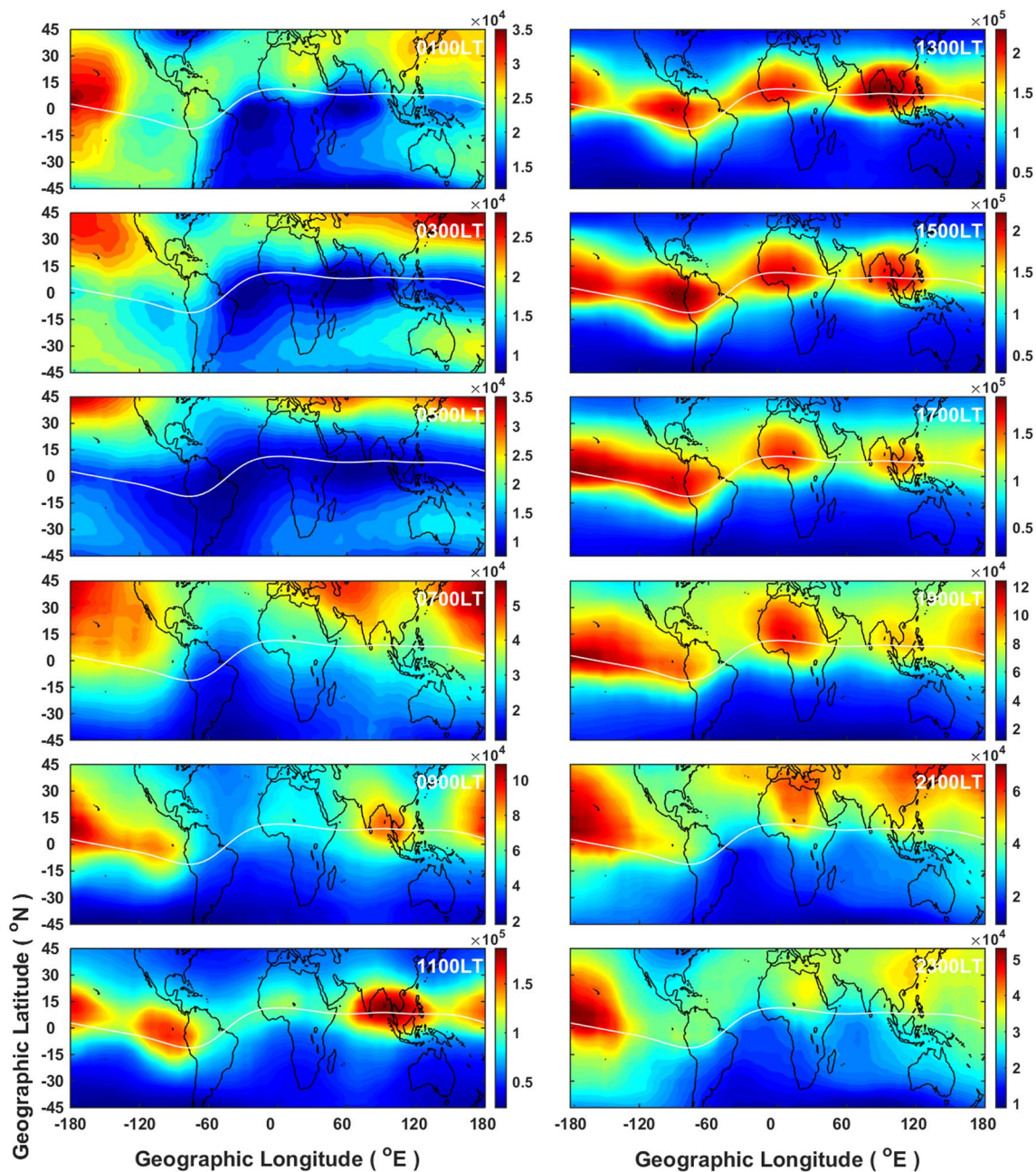


Fig. 4 Diurnal variations of F3/C electron density maps at 450-km altitude at various global fixed local times in September 2008. It is noted that the color contour levels are varying in different subplots in order to clearly show the four-peaked structure. The binning method is same as that used for Fig. 1

tidal decomposition of electron density and/or TEC as well as altitude of the peak electron density (hmF2) for comparisons with the tides at the middle atmosphere. Such attempts focused on identifying the signatures of lower atmospheric variations in influencing the ionospheric electron density distribution, including the longitudinal wave-4 modulation. Pancheva and Mukhtarov

(2010) showed similar local-time variations of longitudinal wave-4/wave-3 patterns in F3/C hmF2 and SABER neutral temperature measurements at 110 km altitude, both demonstrating DE3/DE2 non-migrating oscillations in 2008. The latitudinal and seasonal patterns of DE3 and DE2 were also identical. Moreover, they noted stationary planetary wave (SPW3) contribution in the

wave-3 structure. Chang et al. (2013a) performed an extensive analysis of the TEC extracted from the F3/C measurements during 2007–2011, showing the contribution of DE3, SPW4 and SE2 variations in the wave-4 structures and DE2, SPW3, and SE1 components giving rise to wave-3 features, with SE2/SE1 being relatively less significant; apparently suggesting child waves by aliasing of MLT tides with diurnal ionospheric variability. They show that the wave-4 relative amplitudes are inversely related to the level of solar activity, with little inter-annual variability of the corresponding wave-3 components.

Pancheva et al. (2012) compared the migrating and non-migrating ionospheric oscillations in the F3/C electron density with GAIA model simulations, with both the observations and model results generally agreeing well in representing the spatial structures of the corresponding magnitudes. Such comparisons with F3/C observations are essential to refine the model physics to reflect the complexity of the real-world dynamics, or to explain the measured features based on the model conditions and parameters used. Chang et al. (2013b) examined the amplitudes of migrating diurnal tidal oscillations in the F3/C TEC and pointed out the role of DW1 in contributing to the daytime equatorial peak, SW2 in producing the EIA crests, and TW3 in the equatorial trough. Incidentally, these results suggest that further analysis of TW3 contribution might shed more light on the generation of plasma cave structures mentioned earlier. They further examine the role of upward propagating lower atmospheric tides and the ionospheric non-migrating variability by comparing the results with TIEGCM simulations. The results suggest that DW1 and TW3 ionospheric variability are likely in situ forced, whereas the SW2 response is related to the SW2 forcing in the MLT region, indicating lower atmospheric origin.

Though a number of similar investigations have been carried out following such attempts mentioned above, the remainder of this section will examine the role of F3/C observations in elucidating the intriguing lower atmosphere–ionosphere coupling during SSWs. Unexpected connections have been shown to exist between the equatorial ionosphere and the high-latitude stratospheric variations during SSW (Goncharenko and Zhang 2008; Goncharenko et al. 2010a, 2010b). The EIA shows early morning TEC enhancements followed by the afternoon reduction, with the phase of this diurnal perturbation shifting to later local times on subsequent days. A similar diurnal pattern was confirmed in the peak electron density and altitude by using F3/C measurements over low and mid-latitudes, with the high latitudes exhibiting a consistent increase of electron density (Yue et al. 2010). However, these early analyses did not reveal any longitudinal dependence in the ionosphere variations

during the SSW. Lin et al. (2012a), on the other hand, demonstrate clear longitudinal variation in the local time duration of the electron density increase in the morning / early afternoon sector during SSW by efficiently employing a 20-day moving window to examine the global F3/C electron density maps. Taking full advantage of the F3/C electron density profiles, they further probe the variations of vertical electron density structures during SSW and demonstrate that the longitudinal differences are related to competing SSW induced equatorial plasma fountain variations and the seasonal effects of hemispheric plasma transport, which vary over different longitudes. They also note that the hemispheric asymmetry in the SSW response, with a stronger electron density decrease in the southern hemisphere, may also result from the combined SSW and seasonal effects.

One of the effective ways to examine the coupling between lower at upper atmospheric regions is to examine the tidal components in the neutral and plasma parameters. Pedatella and Forbes (2010) show that the tidal components in the ionosphere are similar to those present in the mesosphere and lower thermosphere (MLT) regions during the SSW period, supporting the hypothesis of the vertical coupling of stratosphere and ionosphere. They provide evidence for the non-linear interactions of planetary waves and tides for the coupling mechanism, where the changing zonal neutral wind plays an important role. Pancheva and Mukhtarov (2011), examining the zonal mean and DW1 variability during the SSW events in 2008 and 2009 based on the tidal decomposition of F3/C electron density, report a negative response in both the components. Lin et al. (2012b) show that the morning-enhancement/afternoon-reduction of the EIA feature could be explained by the phase shift of the diurnal, semi-diurnal, and ter-diurnal migrating tides (DW1, SW2 and TW3), suggesting that the planetary wave responsible to the generation of SSW could alter the global circulations and result in modifications of the migrating tides. The observational evidence reported by Lin et al. (2012b) was later confirmed by the whole atmosphere modeling carried out by Jin et al. (2012). Similar and consistent variations of the amplitude changes and phase shifts of the migrating tidal components also appeared in the F3/C analyses of the ionosphere variations during the three major SSWs in 2008, 2009, and 2010 (Lin et al. 2013).

2.4 Middle latitude trough

Expanding the accomplishments of F3/C RO measurements in the investigation of coupling between lower atmosphere and ionosphere, as well as in detecting new ionospheric structures, the observations has also been applied in studying ionospheric features such as the

middle latitude trough and the Weddell Sea Anomaly. The middle latitude trough is characterized by a narrow longitude belt of a very low electron density region that exists in the mid-latitudes after sunset. It manifests as a persistent large-scale electron density depletion structure that appears in the post-afternoon sector and extends to the dawn sector. It forms as a result of the complex interplay between the eastward co-rotating plasma flow and the westward ion convection flow. Therefore, the middle latitude trough locates at the interface between the mid-latitude ionosphere and the high latitude auroral region (cf. Lee et al. 2011; Chen et al. 2018). Earlier studies could only provide a 2D perspective of the development of the middle latitude trough mainly by using GPS TEC observations from ground-based receiver networks. Owing to global and uniform soundings, the F3/C RO observations provide the best database to examine the global structure of the mid-latitude electron density trough in various local times and seasons.

Lee et al. (2011), for the first time, examined the 3D structure of the time evolution of middle latitude trough and their local-time, seasonal, and magnetic activity dependence. Figure 5, plotted to resemble the illustration adopted by Lee et al. (2011), shows the diurnal variations of NmF2 within 30–80° magnetic latitude in various magnetic local times and seasons. It can be seen that the middle latitude trough is a nighttime phenomenon occurring between 55 and 70° latitudes. Further, the trough shows notable hemispheric asymmetry, becoming more evident in the winter hemisphere. Based on such analysis, Lee et al. (2011) points out that the middle latitude trough is wider than previously known, and the recombination loss in the trough region persists even in the post-midnight period, depleting the plasma density. The unique 3D visualization of the middle latitude trough by using F3/C electron density profiles provides opportunities for better identifying the trough characteristics and further examining the time evolution in detail.

2.5 Weddell and Okhotsk Sea anomaly

The daytime electron density starts to increase as photoionization begins, attains a maximum around 1400–1600 LT, and then decreases with increasing solar zenith angle. On the other hand, once the Sun is set, the electron density falls rapidly in the absence of production, reaching a minimum around 0400–0500 LT. Under this diurnal pattern, the electron density at night is bound to remain smaller compared to the daytime values. Though the general day-night behavior of electron density distribution agrees with this expected pattern, ground-based ionosondes over Antarctica during the International Geophysical Year in the summer of 1957 (Bellchambers and Piggott 1958) indicated an opposite behavior; the

maximum foF2 around the Weddell Sea region occurs at night (2200–0400 LT) instead of during daytime hours (1000–1800 LT). This anomalous behavior in the southern hemisphere was named as Weddell Sea Anomaly (WSA). A similar anomaly is found to exist in the northern hemisphere, appearing prominent near the Europe/Africa and Northeast Asia/Central Pacific longitudes during the June solstice. Since this region is nearby the Okhotsk Sea, the northern hemisphere anomaly is also termed as Okhotsk Sea Anomaly (OSA). From the similarities in the characteristics of these two anomalies as well as their generation mechanisms, both the WSA and OSA anomalies are called midlatitude summer nighttime anomaly or MSNA (Lin et al. 2010). Figure 6a and b illustrate the WSA and OSA (MSNA) features in F3/C electron density, where the difference of noontime (1300 LT) electron density from the nighttime (2300 LT) at 300 km during December (D) and June (J) months in 2009 are plotted. As seen in the figure, in the northern hemisphere, MSNA often exhibits a 2-peak structure.

Lin et al. (2009), for the first time, examine 3D structures of MSNA by using F3/C electron density measurements, and point out that the poleward offset of the magnetic equator from the geographic equator is important in their formation. By examining the monthly mean electron density distributions, Lin et al. (2010) identify similar structures of electron density development in both northern and southern MSNA, where both also show similar poleward displacement of the magnetic equator. Based on the 3D F3/C electron density variations, they propose a plausible generation mechanism as follows. The plasma at the poleward edge of the EIA crest gets transported upward/poleward to nearby higher latitudes by upward $E \times B$ drift occurring around 1800 LT. This plasma merges with newly formed ionization by the remaining sunlight/photoionization and forms an electron density crest at the midlatitude region. In the evening period in the mid-latitude summer hemisphere, meridional winds are predominantly equatorward, which supports this midlatitude electron density crest at higher levels, thus ensuring a longer lifetime. The enhanced electron density regions associated with MSNA occur at around 45° dip angle, where neutral wind driven plasma transport is more efficient in moving plasma along the field lines. As per this mechanism, the MSNA formation is more favorable when the poleward extension of the EIA crests is largest. However, as mentioned in Sect. 2.3, the electron density distribution over the EIA crest latitudes displays a longitudinal wave-3 or wave-4 modulation resulting from the non-migrating tide influence. The locations of these longitudinal peaks of EIA appear over South America, Africa, and Southeast Asia regions. This longitudinal modulation of EIA gives rise to a single

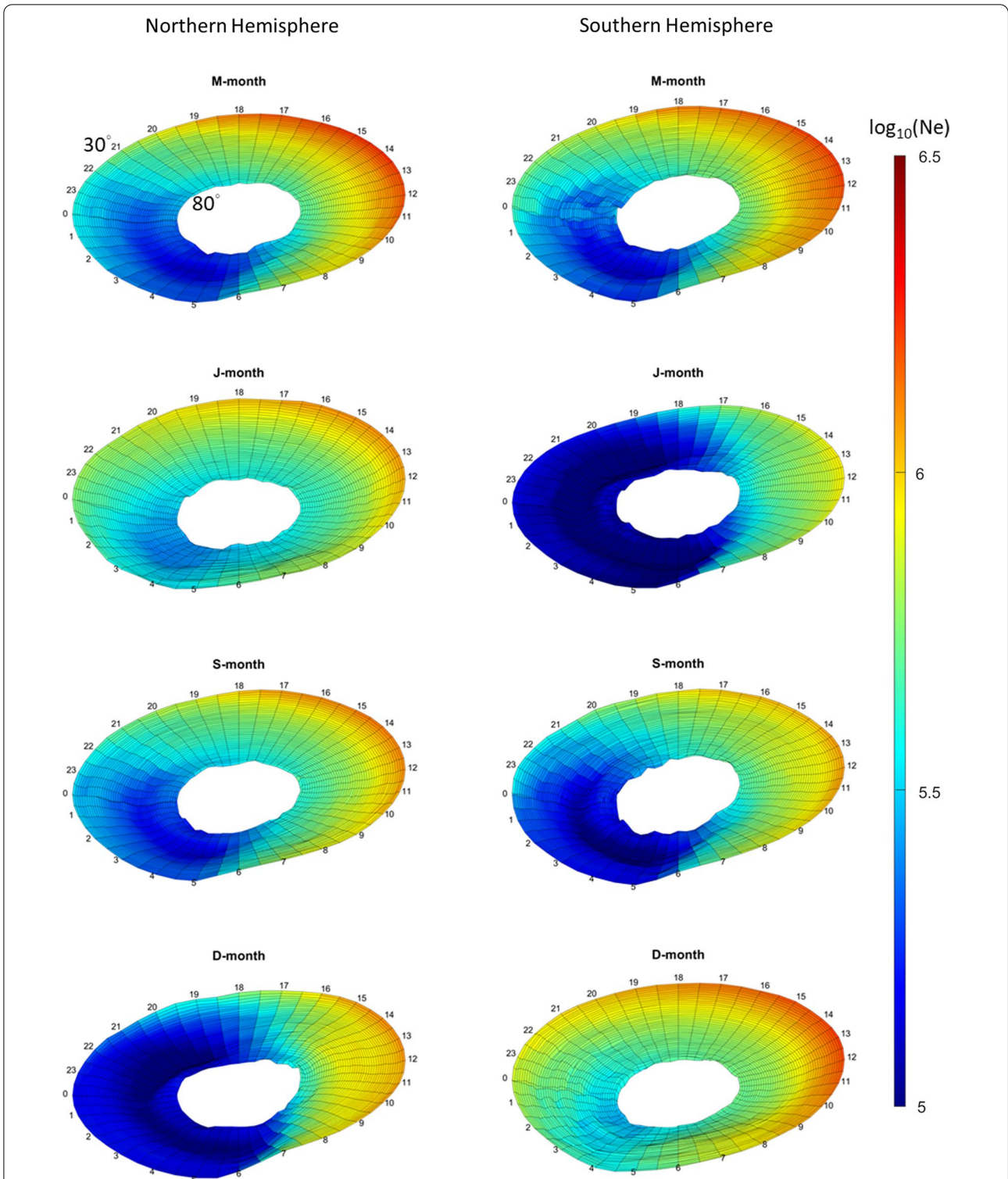
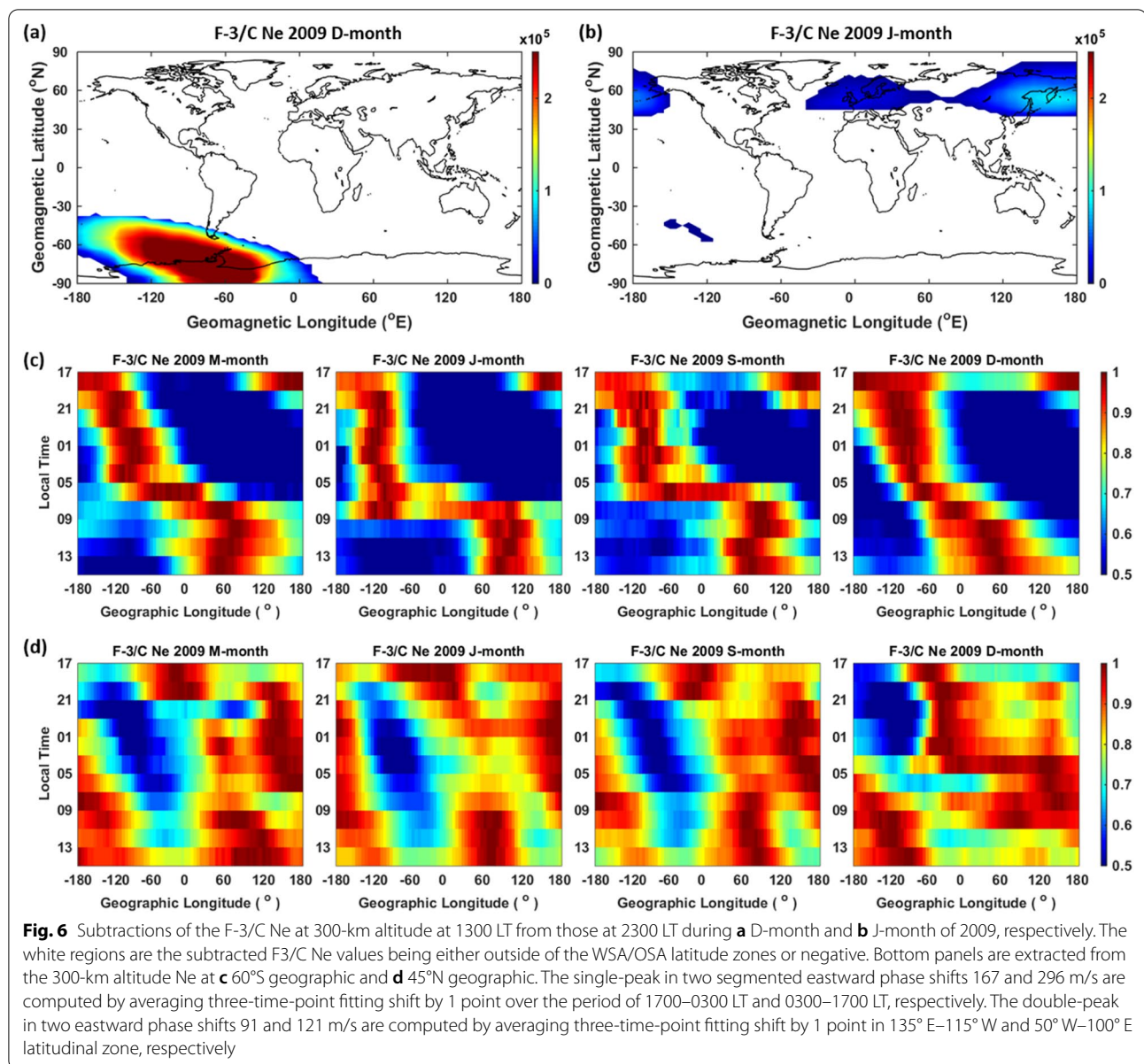


Fig. 5 The seasonal averaged pseudo 3D images of the F2 peak density, NmF2, map from April 2006 to April 2019 in magnetic polar coordinates for the March equinox (M-month), June solstice (J-month), September equinox (S-month), and December solstice (D-month). The inner and outer perimeters are 80° and 30° in magnetic latitude. The left and right columns are results in the Northern and Southern hemispheres, respectively. The color and vertical change refer to the electron density, and the numbers around each plot give the geomagnetic local time. Cell: 0.5 MLT × 1° MLAT. Sliding window: 1-h × 5°. MLT: magnetic local time. MLAT: magnetic latitude



MSNA structure in the southern hemisphere, whereas in the northern hemisphere MSNA might appear to have more than one peak.

Chen et al. (2013) performed simulations of MSNA by using the 3D physics-based ionosphere model, SAMI3, coupling with TIEGCM neutral winds after specifying GSWM (Global Scale Wave Model) tidal forcing at the model lower boundary. The simulations reproduced only single peaks in both northern and southern hemispheres. They attributed this to the fact that TIEGCM neutral winds they used still do not represent the realistic neutral wind variations. Tidal analysis of their simulation results reveals that standing diurnal oscillation (D0) of

the perpendicular component of neutral wind manifests as diurnal eastward wave-1 propagation of MSNA in the fixed local-time frame. On the other hand, Chang et al. (2015) compares three-dimensional F3/C electron density and HWM93 (Horizontal Wind Model 93) simulation and find that the magnetic meridional effect and the vertical effect caused by neutral winds exhibit eastward shifts, which demonstrates that the equatorward and upward effect owing to neutral wind contributions are most essential. Similar to Chang et al. (2015), the F3/C electron density at 300 km altitude over geographic latitudes of 40° to 80° in the Southern hemisphere and 30° to 60° in the Northern hemisphere at various global fixed

local times from February 2009 to January 2010 are plotted in Fig. 6 bottom panels. Figure 6c and d show that an eastward shift of a single-peak plasma density feature occurs along the WSA latitudes, while a double-peak plasma density feature appears along the OSA latitudes in M-month (February~April 2009), J-month (May~July 2009), S-month (August~October 2009), and D-month (November 2009~January of 2010).

2.6 Integrated GOX and TIP observations

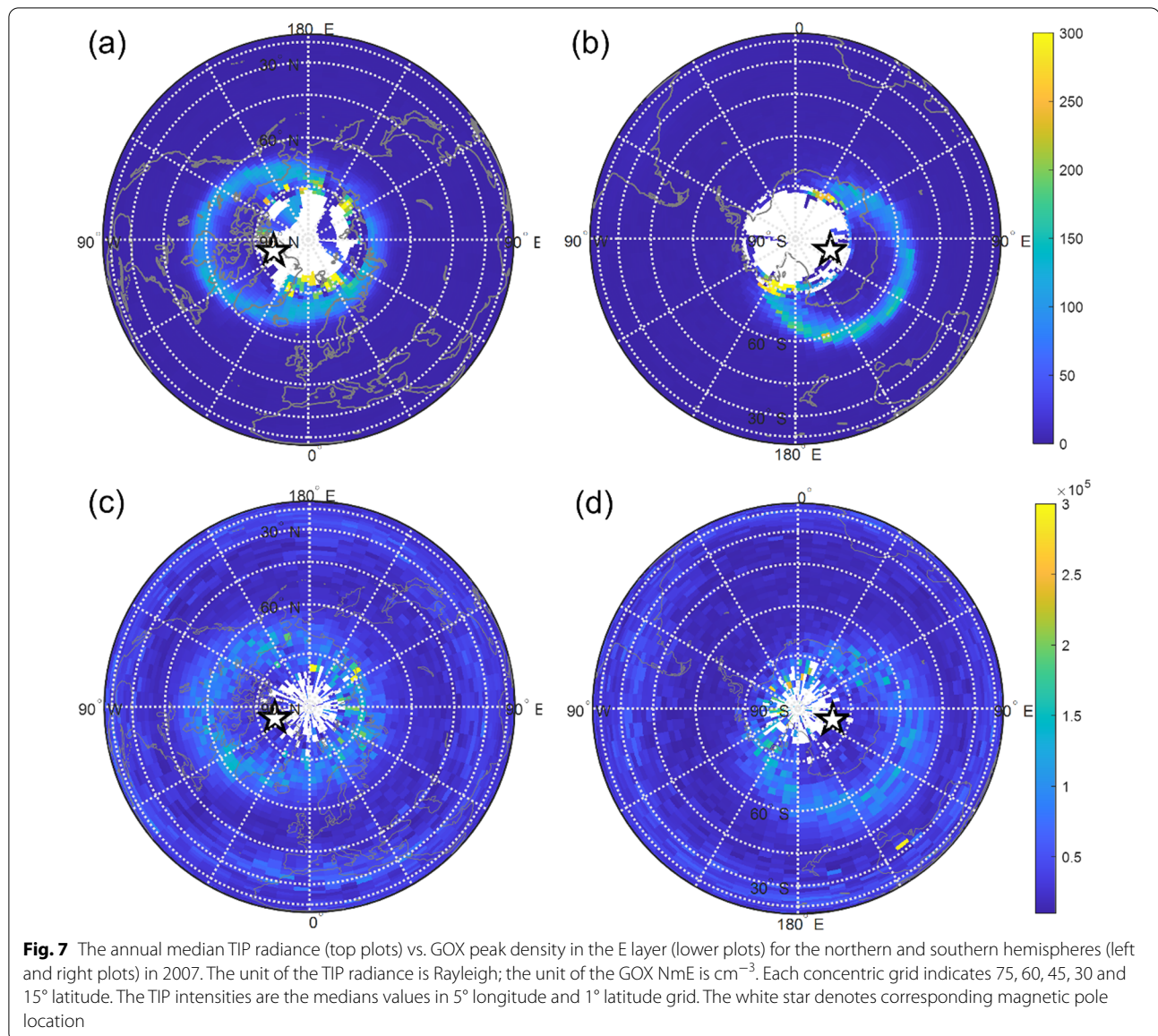
In addition to the RO electron density profiles, the 135.6 nm airglow measurements by TIP have also been used in examining the ionospheric structures. Simultaneous observations of F3/C TIP and GOX have been used to conduct a full space-based (without ground-based receiving stations) ionospheric tomography (Hsu et al. 2009) and to study ionospheric auroral oval development (Tsai et al. 2010). TIP measures nadir integrated OI 135.6 nm intensities, whereas GOX observes the line-of-sight TEC between the F3/C and GPS satellite. While the TEC measurements lack direct information about horizontal gradients of electron density, the high sensitivity of ~600 counts/Rayleigh and a narrow nadir pointing circular field-of-view of 3.8° enables TIP to accurately characterize the ionospheric electron density gradients in the horizontal direction (Chua et al. 2009; Coker et al. 2009; Dymond et al. 2009). Hsu et al. (2009) combined the two observations to carry out full space-based tomographic inversions for the first time and demonstrated that the TIP and GOX data provide more realistic electron density, especially NmF2 and hmF2.

On the other hand, Tsai et al. (2010) utilized F3/C GOX and TIP to study the ionospheric auroral oval development, and to determine the boundaries of the auroral oval and its width in winter nighttime hemispheres in 2007. They found that the auroral oval patterns of the 135.6 nm emission and NmE (maximum electron density at the E-peak) are similar, while the mean width of the auroral bands ranges from 2 to 11° latitudes in the winter nighttime and is longitude dependent in both hemispheres. Results also suggest that the mean radius of the auroral ovals varies with the intensity of the auroral radiance. Figure 7 displays the auroral oval patterns of the 135.6 nm emission of TIP and NmE of GOX in the Northern and Southern hemispheres in 2007. The TIP radiance (panels (a) and (b)) and GOX NmE layer (panels (b) and (c)) show clear images of the auroral ovals between 55–70°N and 50–85°S, around magnetic poles. This indicates that auroral precipitations result in prominent enhancements of 135.6 nm emission around the F2-peak and significant percentage increases of the electron density in the E region.

2.7 Ionospheric earthquake and tsunami disturbances

One of the unique applications of the vertical profiles from F3/C RO measurements is to examine and understand the electron density variations that co-exist and/or persist during major earthquake events. An earthquake produces overwhelming Earth surface motions and induce devastating tsunamis if occurs offshore, which then travel into the ionosphere and significantly disturb its electron density. Scientists have observed ionospheric disturbances by means of TEC of ground-based GPS receivers and space-based radio occultations (cf. Liu et al. 2006, 2010b, 2011a, b; Sun et al. 2016). It should be noted that the F3/C space-based RO experiment is not a dedicated mission to detect the signatures of such seismic disturbances. On the other hand, such measurements are hand-picked when the occultations occur at the “right location and time” during such events. This section and the next are intended to provide an illustration of how such available resources can be efficiently employed as very effective tools in providing valuable information, which are useful not only for the scientific community, but are in the best interests of the general public and government agencies as well. The descriptions below are adopted from the published work by Liu et al. (2019) since such events are rare and not many examples are available to re-produce the results.

A destructive giant M9.0 earthquake occurred around Tohoku, Japan (38.3°N, 142.4°E), at 05:46:23 UT on 11 March 2011, triggering large tsunami waves that swept over the island nation, causing widespread damage and loss of life. The atmospheric disturbances produced by the earthquake and the tsunami propagation produce horizontal and vertical modulations in the ionosphere electron density distribution. A number of F3/C RO events that occurred around the region affected by tsunami waves are used to investigate the fluctuations on vertical electron density profiles induced by the Tohoku earthquake and tsunami (Liu et al. 2019). Figure 8a displays the locations of 22 (7 before and 15 after) F3/C vertical profiles within a 3000 km in radius from the epicenter during the earthquake. Fluctuations of the electron density profile induced by Rayleigh and tsunami waves and the post-wave disturbances are examined. The fluctuations produced by Rayleigh waves and tsunami waves on the vertical electron density profiles are distinguished by examining the differences in the arrival times of the wave disturbances. Figure 8b shows that the right underneath Rayleigh wave can induce significant long-wavelength fluctuations of 50–105 km on the vertical profile of the electron density (Profile#11 & #12), while tsunami and their post-waves activate the prominent short-wavelength fluctuations less than 16 km on those profiles (Profile#15, #16 and Profile#18, #19, #22,

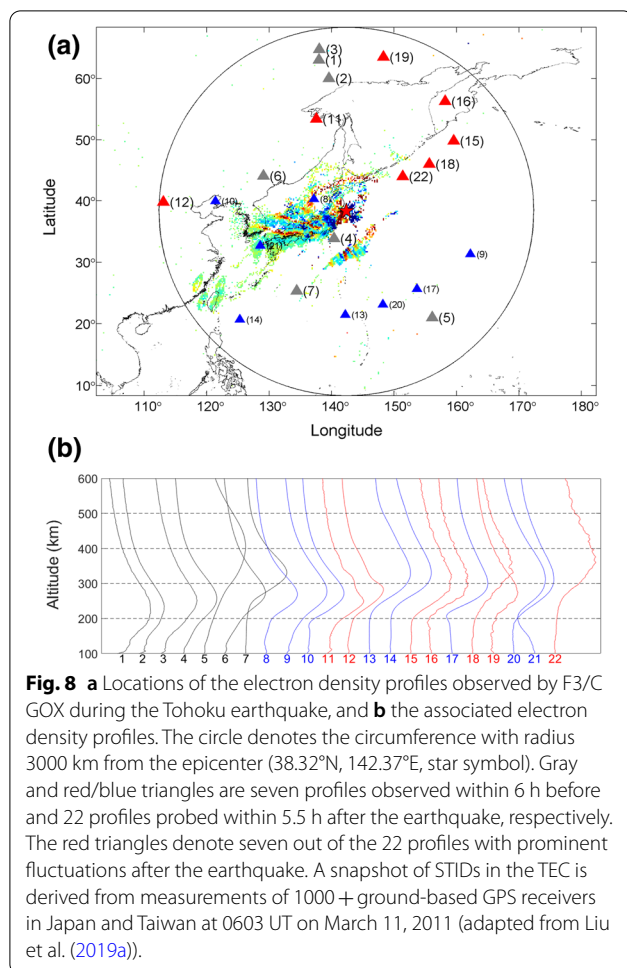


respectively) in the poleward side of the epicenter. These results show that radio occultation can be a powerful tool that is suitable to probe vertical fluctuations in the ionospheric electron density.

3 Ionospheric weather models

The preceding sections mainly cover some of the specific topics where the F3/C observations have contributed to advancing the existing understanding, while also revealing new and exciting features. On the other hand, the enormous number of ionospheric measurements made by the F3/C satellites over the past 14 years, which far exceeded the expected mission lifetime, are also applied to achieve another important mission goal of

understanding/predicting ionosphere weather and ionosphere climate. Variations of ionospheric electron density distribution can adversely affect numerous human activities and systems, such as disrupting communications systems, degrading the performance of navigation and reconnaissance systems (e.g., Boteler 2001; Lanzerotti 2001; Baker et al. 2004; Roy and Paul 2013; Thaduri et al. 2020) These variations are also referred to as ionospheric weather. Currently, space weather centers have been set up in many countries to monitor and forecast space weather changes. However, until recently, realistic ionospheric weather forecast modeling had been challenging due to the lack of sufficient data coverage, especially over oceanic and remote areas, with only limited satellite



observations being available. The F3/C RO profiles presented the best chance to overcome this limitation, providing 3D structures of electron density and scintillation, and for the first time making the ionospheric weather monitoring, nowcast, and forecast feasible.

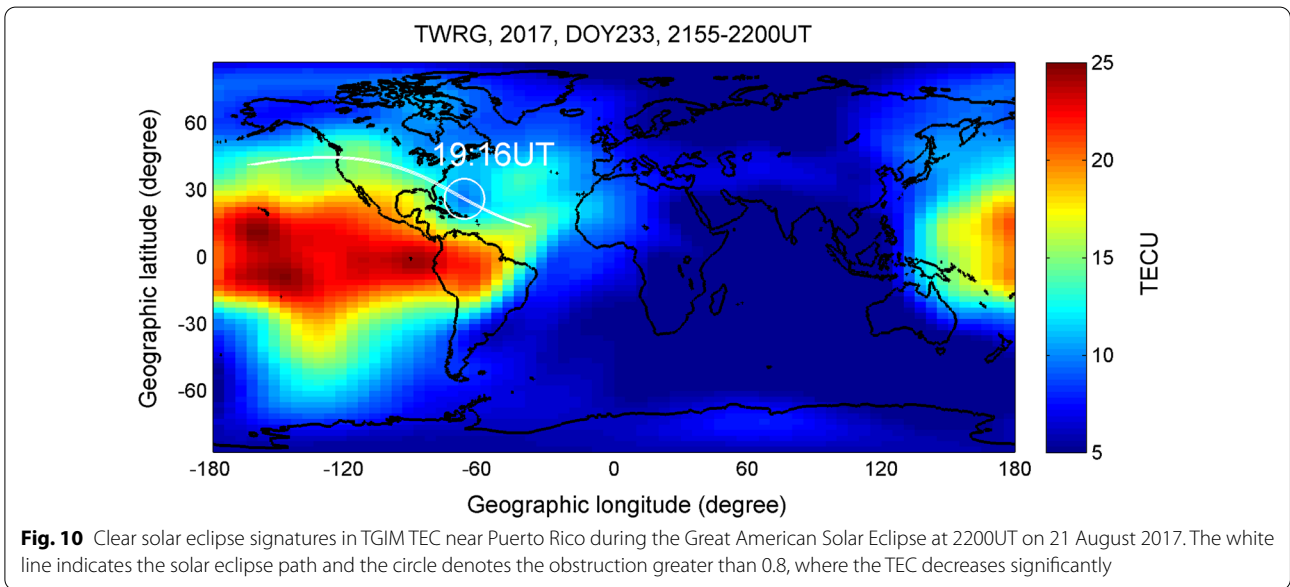
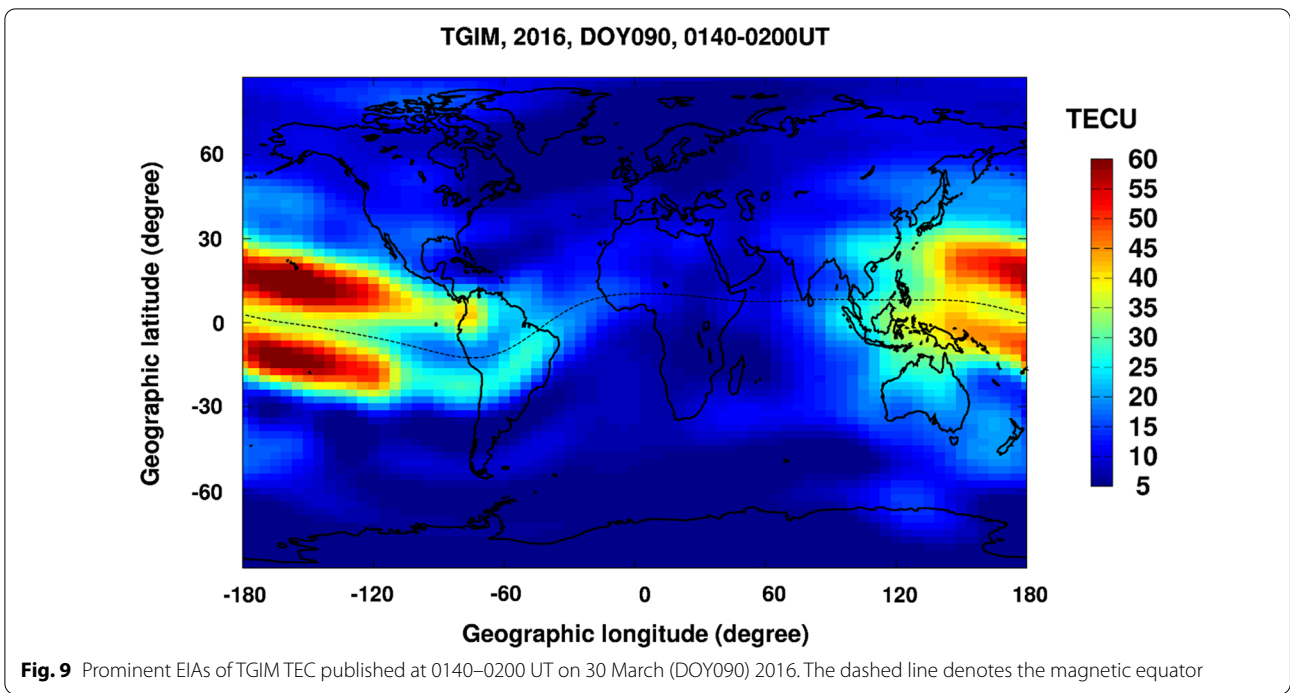
3.1 Ionospheric weather monitoring

Based on measurements of ground based GNSS networks, the GIM of TEC is constructed and published by several institutes/organizations/companies (Sun et al. 2017). However, these existing GIMs mainly collect TEC from the ground-based receivers over continental regions, which results in less accuracy over the ocean and remote areas, such as desert and polar regions. The F3/C satellites observe RO electron density profiles globally and record plasmaspheric electron content (PEC) above satellite orbit altitude by receiving signals of non-occultation GPS satellites. The PEC can further add integral electron content by integrating the co-located RO electron density profile, then forming similar observations as ground-based GNSS TEC. The Taiwan Ionospheric

Group for Education and Research (TIGER) at National Central University (NCU) developed an advanced product by combining the PEC and global GNSS TEC data, which was named the TIGER GIM (TGIM) (Sun et al. 2017). Sun et al. (2017) show that the F3/C RO data (i.e., PEC) significantly improves the TGIM over the ocean areas, especially in the Southern Hemisphere, which allows scientists to study the ionospheric weather-related to solar flares, solar eclipses, magnetic storms, sudden stratospheric warming, mid-latitude summer night anomaly, and lithosphere–atmosphere–ionosphere coupling. The TGIM is currently being operated by the Taiwan Analysis Center for COSMIC (TACC) and the Space Weather operational Office (SWOO) of Central Weather Bureau, Taiwan, publishing hourly TEC maps with a 4-h time delay. (<https://swoo.cwb.gov.tw/V2/page/EN/Observation/IonoTECmap.html>). The TGIM is constructed by using about 100 IGS stations and RO data in near-real time with a standard spatial resolution of 2.5° in latitude and 5° in longitude, and 5-min temporal resolution. Figure 9 shows prominent EIA signatures in TGIM TEC appearing at 0140–0200 UT on 30 March (DOY090) 2016, while Fig. 10 illustrates clear ionospheric effects occurring near Puerto Rico during the 21 August 2017 solar eclipse. The maximum Moon’s umbral shadow passed over this area around 19:16 UT and yielded a clear circular depletion of TEC a few hours later. These two figures show that TGIM is useful for near-real-time positioning and navigation applications as well as scientific researches.

3.2 Ionospheric weather nowcast

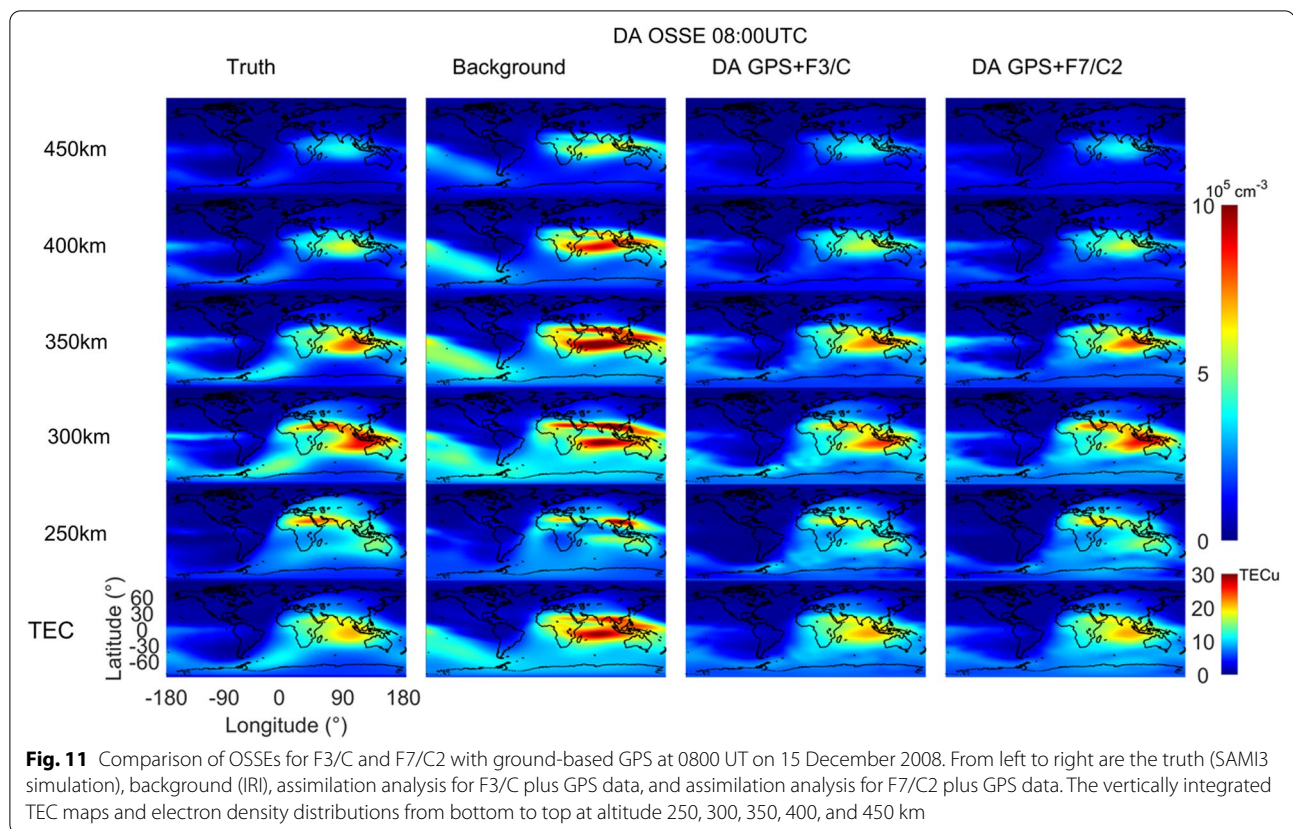
To observe near real-time global 3D electron density structures and dynamics, the ionospheric weather nowcast model named Global Ionospheric Specification (GIS) has been developed (Lin et al. 2015, 2017). The GIS assimilates ground based GNSS and LEO RO TEC measurement by using a Kalman filter (Kalman 1960; Kalman and Bucy 1961) to reconstruct the global electron density structure. The Kalman filter, a recursive algorithm composed of measurement update and forecast steps to provide an optimal solution to a dynamical state estimation, is one of the commonly used approaches in ionospheric data assimilation. The GIS grid resolutions are 2.5° in latitude, 5° in longitude, and 20 km in height extending from 100 to 1000 km, and the time resolution is 1-h. The Kalman filter measurement update implemented in GIS and the methods to calculate the background model error covariance and observation error covariance are described by Lin et al. (2015). The forecast procedure in GIS is refined to use linear Gauss-Markov model to evolve the assimilation analysis from the current time step to the next time step by longitudinally shifting



ionospheric electron density in geomagnetic coordinates at the rate of the Earth's rotation as well as a relaxation to the climatological background ionosphere (Lin et al. 2017).

OSSEs (Observing System Simulation Experiments) for assimilating ground-based GPS data and RO data (F3/C or F7/C2) are conducted to examine the quality of data assimilation analysis. Figure 11 shows the vertical TEC

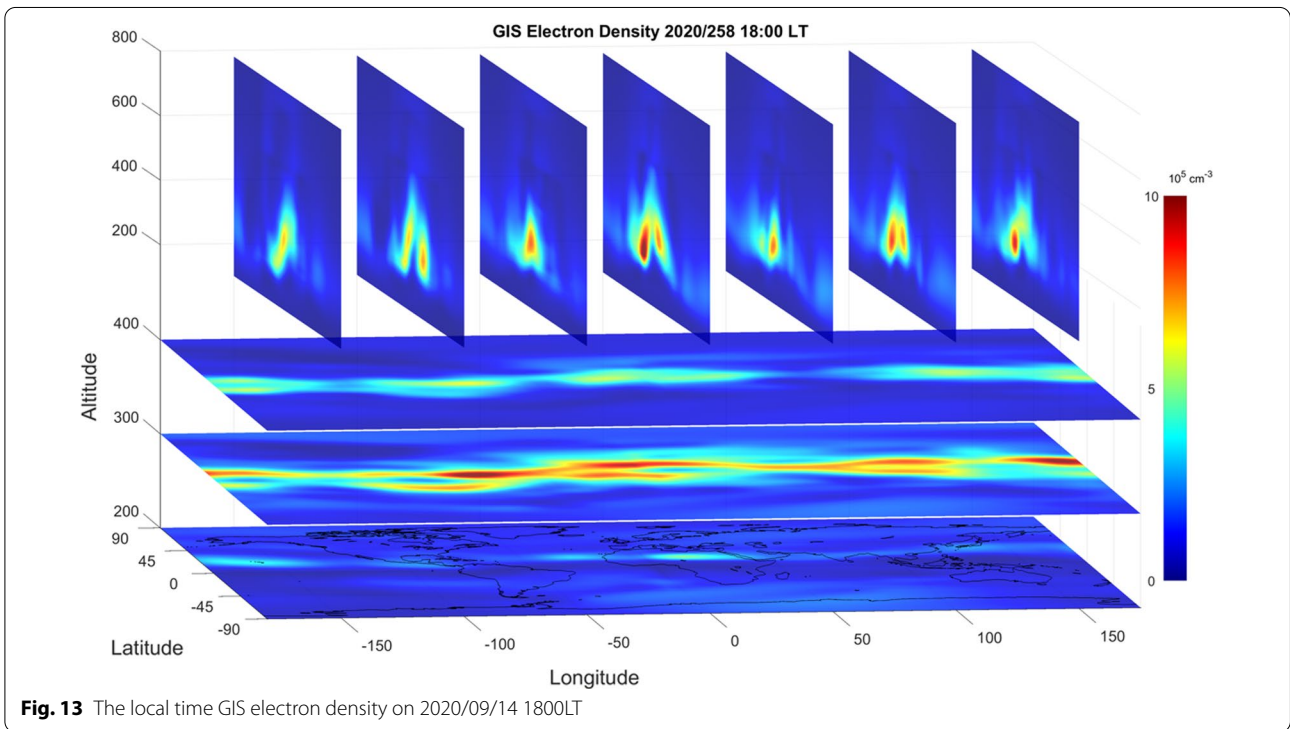
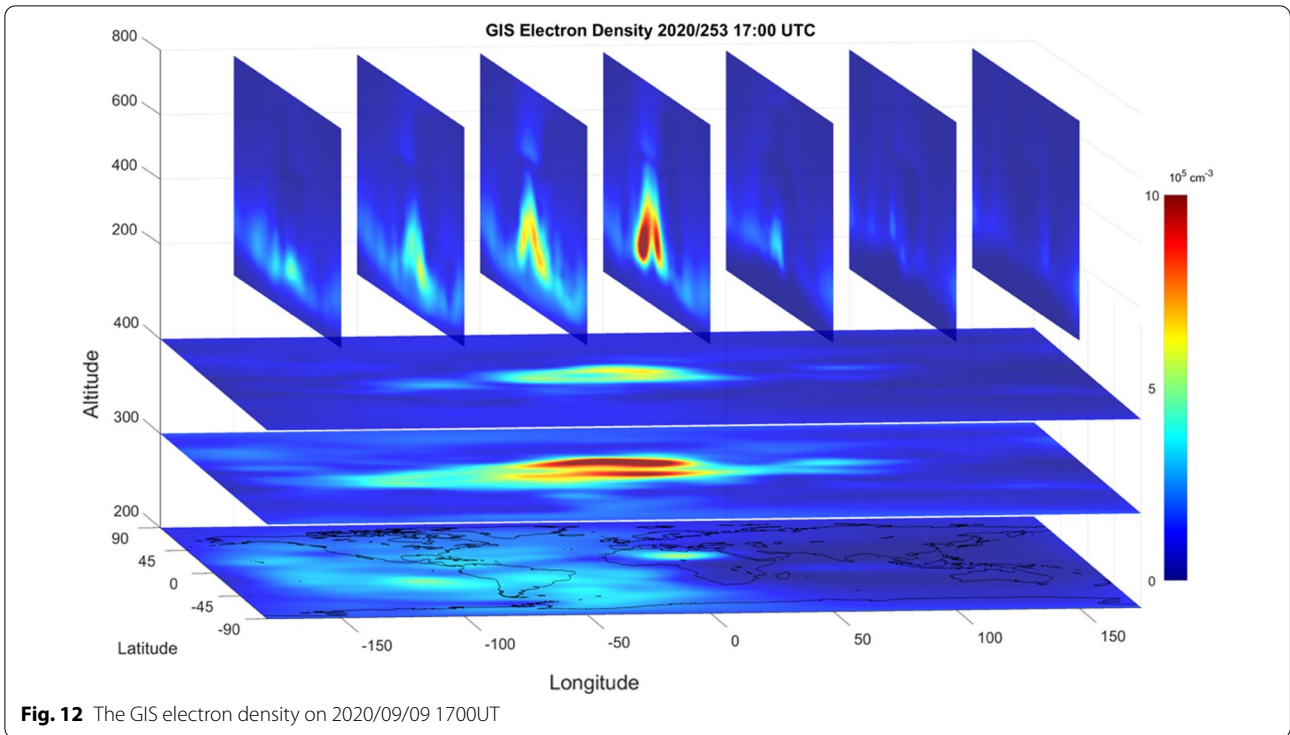
(bottom panel) and the electron density maps at every 50 km over 250–500 km altitudes at 0800 UT from the OSSE. The assimilation truth or nature ionosphere (using SAMI3 simulation) is given in the first column and the background or initial ionosphere (using IRI model) is given in the second column. The assimilation results for F3/C and F7/C2 RO inputs are respectively given in columns 3 and 4. The performance of the assimilation



depends on how good it can reproduce the simulation truth compared to the initial background ionosphere used. It can be seen from results that, for both the F3/C and F7/C2 assimilations, the outputs bear no resemblance to the initial background ionosphere but appear as a replica of the nature ionosphere truth, demonstrating how well the actual global electron density distribution is reproduced from the ground- and space-based slant TEC measurements. A careful comparison of the F3/C and F7/C2 outputs with the simulation truth reveals that F7/C2 performs slightly better than F3/C in re-producing the EIA distribution. This better performance of the assimilation with F7/C2 over the EIA region compared to F3/C could be because of the much denser data sampling by the former. See Liu et al. (2022) for further details regarding the advantages of the performance of F7/C2. The OSSE results demonstrate the potential of GIS in reconstructing daily 3D global electron density distribution.

Lin et al. (2020b) validated GIS by independent digisonde manual scaling data and found that comparisons of NmF2 and hmF2 between digisonde and GIS have high correlation coefficients. These OSSEs and validation confirm that GIS has the capability to reconstruct well-resolved electron density structures. Figures 12 and 13 depict two significant EIA crests on 2020/09/09 1700UT

and the wave number 4 structure at 300 and 400 km altitude on 2020/09/14 1700LT, demonstrating that GIS can reconstruct ionosphere in longitudes (wave-4) and latitudes (EIA crests), respectively. Furthermore, Lin et al. (2019a, b) used GIS to investigate the ionospheric day-to-day tidal variability during the 2009 SSW period, showing the combined effect of semidiurnal migrating tide and M2 lunar tide for generation of the beats of the 12-h ionosphere oscillation. Lin et al. (2020a) reported new characteristics of ionospheric modulations driven by the quasi-6-day wave (Q6DW) burst following a rare Antarctic SSW occurred in September 2019 using GIS electron density. They found that the 30% amplitude of ionosphere oscillation driven by the SSW-related Q6DW is much greater than the typical 10% amplitude of the ionosphere quasi-6-day oscillation during other years. Rajesh et al. (2021a) examined the ionospheric response to a minor magnetic storm using GIS electron density, and the results reveal $\sim 300\%$ enhancement of EIA crests. These studies indicate that GIS is reliable ionospheric weather nowcast product in studying space weather research and day-to-day variations. The strong variability of ionosphere comes not only from special events like SSW or storms but also lower atmospheric forcing. Rajesh et al. (2021b) investigated the day-to-day variability of



the mid- and low-latitude ionosphere using GIS during a deep solar minimum period of August 2019 to July 2020. The results showed significant daily variations over

dayside low latitudes, yielding about 10–20% standard deviation in equinoxes, 20–30% in solstices, reaching 40–50% in winter.

These literature show that the GIS can be employed to nowcast the global 3D electron density structures of space weather. Currently, GIS is being published at 0000 UT daily by SWOO (<https://swoo.cwb.gov.tw/V2/page/EN/Observation/IonoMonitor.html>).

3.3 Ionospheric weather forecast

The Numerical Weather Prediction (NWP) was originally developed to predict tropospheric weather based on the current atmospheric conditions constrained with observations by means of data assimilation. Scientists attempted to predict tropospheric weather in the early nineteenth century, and the first operational NWP system was achieved in 1958 (cf. Shuman 1989). In contrast, the need to develop such a NWP system for ionosphere weather was not recognized until the twentieth century. Several ionospheric data assimilation models have been proposed over the past two decades, including two Global Assimilation of Ionospheric Measurements (GAIM) models developed independently by the Utah State University and the team of the University of Southern California and Jet Propulsion Laboratory (e.g., Pi et al. 2003; Hajj et al. 2004; Heelis and Howe 2004; Schunk et al. 2004; Scherliess et al. 2009) as well as the National Center for National Atmospheric Research (NCAR) Data Assimilation Research Testbed/Thermosphere-Ionosphere-Electrodynamics General Circulation Model (DART/TIE-GCM) (e.g., Matsuo and Araujo-Pradere 2011; Lee et al. 2012b, 2013; Matsuo et al. 2013).

The DART/TIE-GCM is a coupled thermosphere/ionosphere data assimilation system that can self-consistently take electrodynamic processes between neutral and charged states into account. The capability of the DART/TIE-GCM to improve ionospheric space weather prediction by assimilating the F3/C and F7/C2 has been examined in the past years. Lee et al. (2012b) first assimilated the F3/C electron density profiles into the TIE-GCM to adjust the modeled electron density distribution. They have shown that the NmF2 and hmF2 obtained by assimilating the RO electron density profile observations agree better with ionosonde observations than those from the default TIE-GCM simulations. The electron densities in most regions have been improved during geomagnetically quiet time conditions, as well as in the daytime high-latitude region under highly geomagnetically disturbed conditions.

The ionospheric weather condition is dominated by external drivers, which involve solar radiation, high-latitude electric fields, and auroral particle precipitation, and affected by initial conditions of the ionospheric and thermospheric state, which involves electron density, atomic oxygen ion density, thermospheric compositions, neutral temperature, and neutral winds. Hsu et al.

(2014) have found that adjusting these thermospheric state variables in addition to the ionospheric state variables by data assimilation of the F3/C electron density profiles can improve the ionospheric predictability in comparison to adjusting only ionospheric variables. They have shown that the thermospheric composition is the most significant state variable that has a great impact on increasing the accuracy of ionospheric forecasting by the DART/TIEGCM. Thus, the assimilation system based on a thermosphere-ionosphere coupled model can yield ionospheric numerical weather forecasting capabilities beyond the system that employs an ionospheric model. Lee et al. (2013) and Hsu et al. (2018a, 2018b) have further shown that in addition to F3/C, assimilation of the F7/C2 RO observations into thermosphere-ionosphere coupled models facilitates ionospheric weather forecasting.

The advantage of assimilating ionospheric electron density data into a thermosphere-ionosphere coupled model has been demonstrated by a series of studies. Chen et al. (2016a, 2016b) have assimilated worldwide ground-based GPS TEC observations into the DART/TIE-GCM system, and investigated effects of various assimilation-forecast cycle lengths under the geomagnetic disturbance period. Results showed that in addition to F3/C, GPS TEC observations can be successfully assimilated, and that a shorter assimilation-forecast cycling time and the use of the Weimer high-latitude empirical model in the TIE-GCM would bring the modeled ionospheric density closer to reality. More recently, the DART/TIE-GCM was employed to modify the ionospheric dynamo electric fields through adjusting the thermospheric neutral winds based on the correlations between the assimilated ionosphere parameters and the thermospheric winds (Chen et al. 2017a, b). It was found that the modified electric fields are more consistent with the ground-based radar observations in comparison to the electric fields from the default TIE-GCM simulation, highlighting the ability of the DART/TIE-GCM to extend the forecasting capability of thermosphere-ionosphere models. Furthermore, the DART/TIE-GCM system was used to investigate the global current system changes due to the 2017 solar eclipse event and showed the disturbance clockwise current in the southern hemisphere and counterclockwise current in the northern hemisphere driven by the conductivity discontinuity due to the eclipse are responsible for the formation of the equatorial ionospheric anomaly at earlier times (Chen et al. 2019).

Following such modeling efforts, the Space Weather Operational Office/Center Weather Bureau (SWOO/CWB <https://swoo.cwb.gov.tw/V2/>) and Space Weather Prediction Center/NOAA (<https://www.swpc.noaa.gov/products/wam-ipe>) are currently conducting ionospheric

weather forecast. The DART/TIE-GCM has been routinely run at the SWOO/CWB since 2020 and produces 6-h ionospheric forecasting with hourly outputs (<https://swoo.cwb.gov.tw/V2/page/EN/Forecast/IonoForecast.html>). Figure 14 depicts the global ionospheric weather for 6-h forecasts of TEC, NmF2, hmF2, and foF2 at 0600 UT on 31 August of 2021. Figure 15 illustrates comparisons between assimilated results together with their 6-h

forecasts of foF2 and NmF2 and those observed by the local ionosonde in Taiwan during 10–11 August 2021. The agreements in foF2 and NmF2 of the assimilation output and ionosonde observations show that the forecast model can be employed for ionospheric weather prediction.

The Advanced Ionospheric Probe (AIP) onboard the FORMOSAT-5 satellite and the Ion Velocity Meter

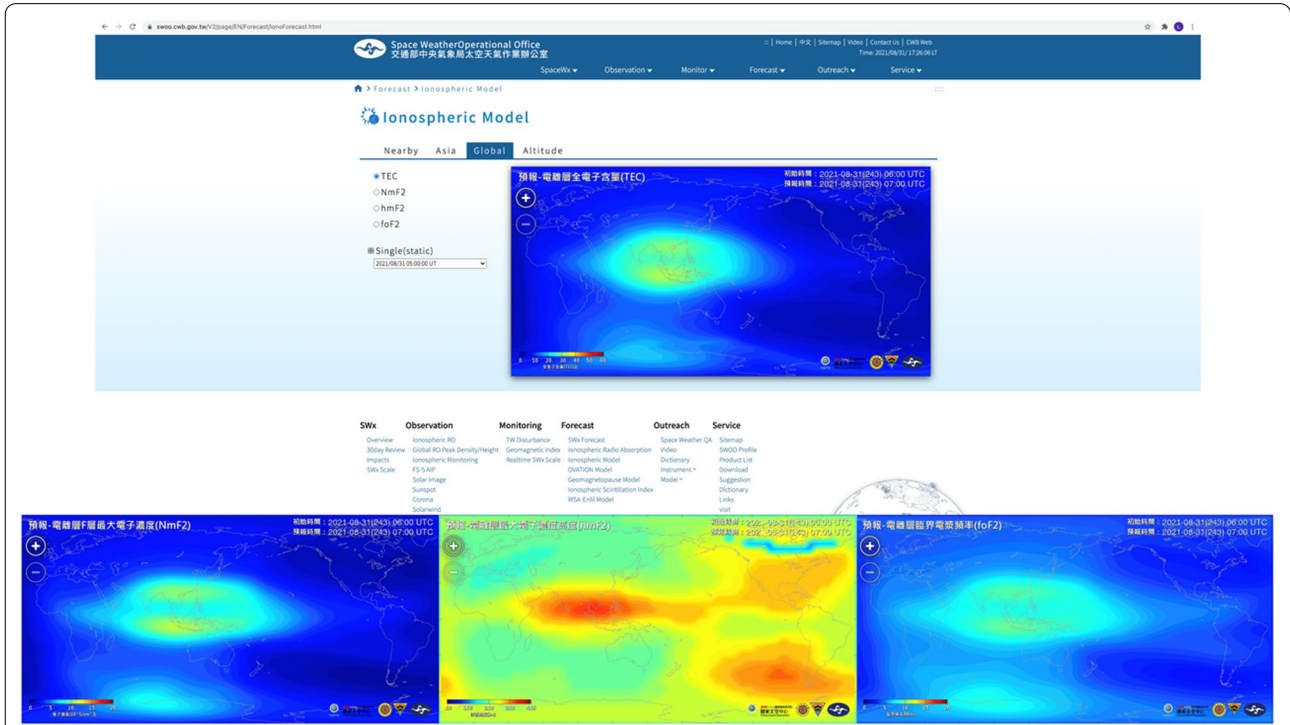


Fig. 14 The global ionospheric weather for 6-h forecasts of TEC, NmF2, hmF2, and foF2 at 0600 UT on 31 August of 2021

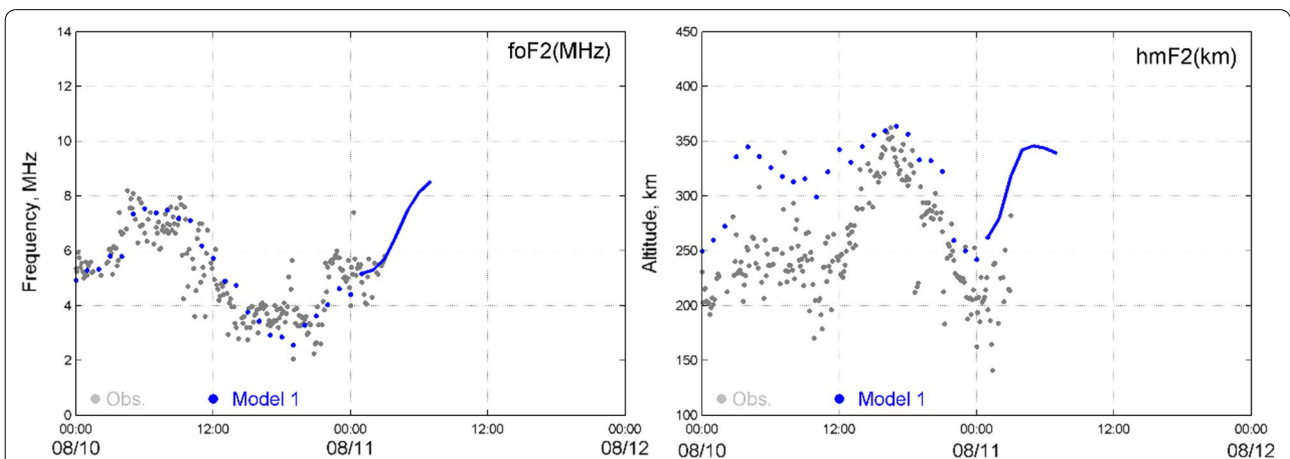


Fig. 15 Comparisons between assimilated results together with their 6-h forecasts of foF2 and NmF2 and those observed by a local ionosonde in Taiwan during 10–11 August 2021

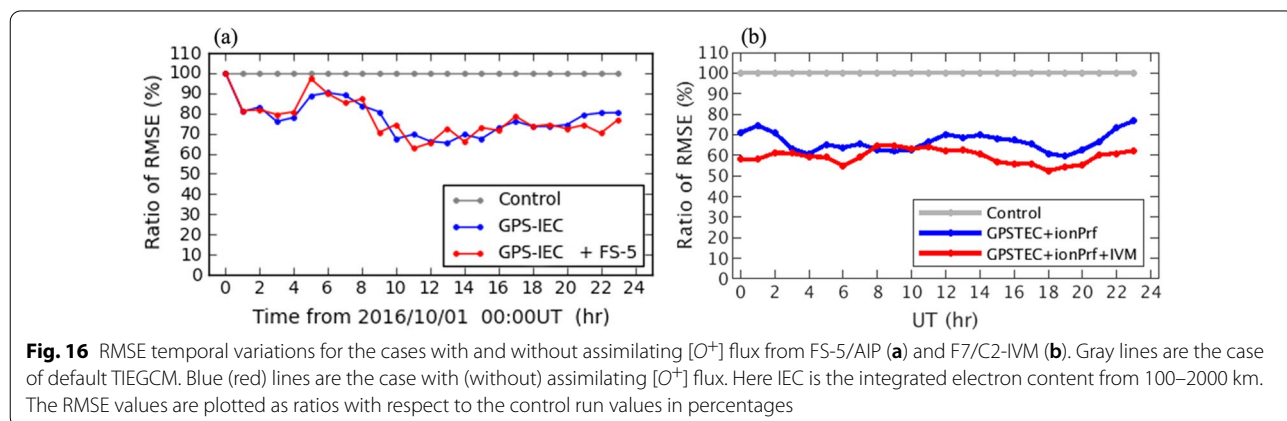
(IVM) onboard the F7/C2 constellation satellites observing the in-situ [O+] density and velocity at ~720 km and ~550 km altitude, respectively, can provide important information at the upper boundary region of the TIE-GCM. Currently the TIE-GCM solves oxygen ion density by specifying a simplified empirical model of [O+] fluxes at the upper boundary of 500~800 km altitude depending on solar activity. The empirical [O+] fluxes at the upper boundary of TIE-GCM is a function of geographic coordination ranging from -2×10^8 to $2 \times 10^8 \text{ #cm}^{-2} \text{ s}^{-1}$. This boundary condition strongly controls the model forecast accuracy (Chen et al. 2016c). To evaluate the impact of [O+] flux obtained from FS-5/AIP and F7/C2-IVM on the performance of the ionospheric weather forecast model, a set of OSSEs were carried out by using the SAMI3 model (Huba and Joyce 2010). Figure 16a displays that the improvement of ionospheric electron density forecasting is around 20–30% in terms of root-mean-square-error (RMSE) by assimilating GPS-TEC and FS-5/AIP observations. However, there is no clear impact on the space weather forecast from the assimilation of FS-5/AIP observations during nighttime (Chen et al. 2016c). F7/C2, constellated by six satellites could provide more [O+] flux observations than FS-5 alone around low and middle latitudes and is expected to generate positive improvements. The RMSE in Fig. 16b illustrates that the assimilation of GPS-TEC and F7/C2-IVM observation can greatly improve the TIE-GCM electron density by about 40%. Among these, the assimilation of F7/C2-IVM provides at least 10% improvement in the initial 2-h of forecast. The real world F7/C2-IVM observations is expected to improve the forecast accuracy and extend the numerical prediction of space weather.

3.4 Ionospheric L-band S4 scintillation

Apart from the remarkable contributions of F3/C in investigating the background ionospheric morphology

and monitoring daily electron density distributions as well as in greatly improving ionosphere forecast models, another very significant field of application of the RO observations is in examining the ionospheric irregularities, especially in the low latitudes. Despite several decades of observations and analysis, developing the capability to forecast the occurrence of irregularities is still challenging due to the lack of regular global measurements (Secan et al. 1995; Anderson and Redmon 2017). Space based observations, to some extent, overcome this limitation, offering global climatological patterns of irregularity occurrence (e.g., Gentile et al. 2006), helping to improve the estimates of the occurrence probability (Huang et al., 2014). With the vast global coverage, the F3/C observations further facilitated the global monitoring of irregularities by detecting the scintillation index S4 (S4-index) derived from the SNR (signal-to-noise ratio) intensity of receiving GNSS L1-band (1.575 GHz) C/A code in the F3/C scnlv1 data (Syndergaard 2006). Note that the radio signals scatter when the ray encounters the plasma irregularities causing the reduction/fluctuation of receiving signal intensities, which are termed as radio scintillation.

The F3/C scintillation measurements have extensively used to examine the distribution of sporadic-E (Es) layers (e.g., Wang et al. 2009; Brahmanandam et al. 2012; Tsai et al. 2018). The studies revealed good comparison of the observed Es altitudes with those from ground-based measurements. Further, the results showed strong seasonal and inter-annual fluctuations in Es layer activity, with the occurrence maximizing in summer months (Arras et al. 2008; Arras and Wickert 2018). The altitude of Es maximum was found to be at about 102 km, with the latitude peak of occurrence around 40–45°. The Es layer occurs at relatively higher altitude at mid-latitudes than over the low latitudes. Such studies also found that the thickness and density of the Es layer are related



(Arras et al. 2008; Qiu et al. 2021). Arras et al. (2009) showed a strong correlation in the local-time variation of Es and semi-diurnal tide in zonal wind shear. The F3/C observations further demonstrated the roles of meteor activity and wind shear in the generation as well as in the hemispheric asymmetry of sporadic-E layers (Yeh et al. 2014). Chang et al. (2018) demonstrated that the Es layer variations could carry the signatures of El Niño–Southern Oscillation (ENSO) in the troposphere based on the dependence with the tropopause height variations and suggested that vertically propagating tides modulate the lower thermospheric wind shears that generate the Es.

In addition to examining characteristics of Es layer, the S4 index retrieved from the F3/C measurements are also used to examine the global and seasonal distribution of F-region plasma irregularities (Ko and Yeh, 2010; Brahmanandam et al. 2012; Uma et al. 2012; Liu et al. 2016a, b; Tsai et al. 2018). Such studies, for the first time, offered global occurrence maps of ionospheric irregularities, also revealing their altitude distributions, showing that the occurrence peaks around 250–300 km. Brahmanandam et al. (2012) noted a suppression in the S4 activity during geomagnetically disturbed periods, in accordance with previous measurements. Long-term observations revealed a strong solar activity dependence in the vertical spread of the S4 occurrence (Kepkar et al. 2020). They also reported that in solar maximum, the S4 occurrence peaked around 2100 LT, and is delayed by about an hour in solar minimum. Chou et al. (2020) examined the background ionospheric conditions that influence the seasonal and solar cycle variations of S4 distribution, reporting the magnetic declination control in the seasonal pattern, cautioning that hemispherical asymmetry of EIA patterns can alter this seasonal behavior. They demonstrated a possible link between eastward propagating non-migrating tides in the climatology of plasma irregularities, based on the wave-3/wave-4 pattern in the longitude distribution, which is pronounced during low solar activity. They also showed evidence for gravity waves pre-conditioning the bottom-side F-region, producing upwelling prior to the generation of irregularities.

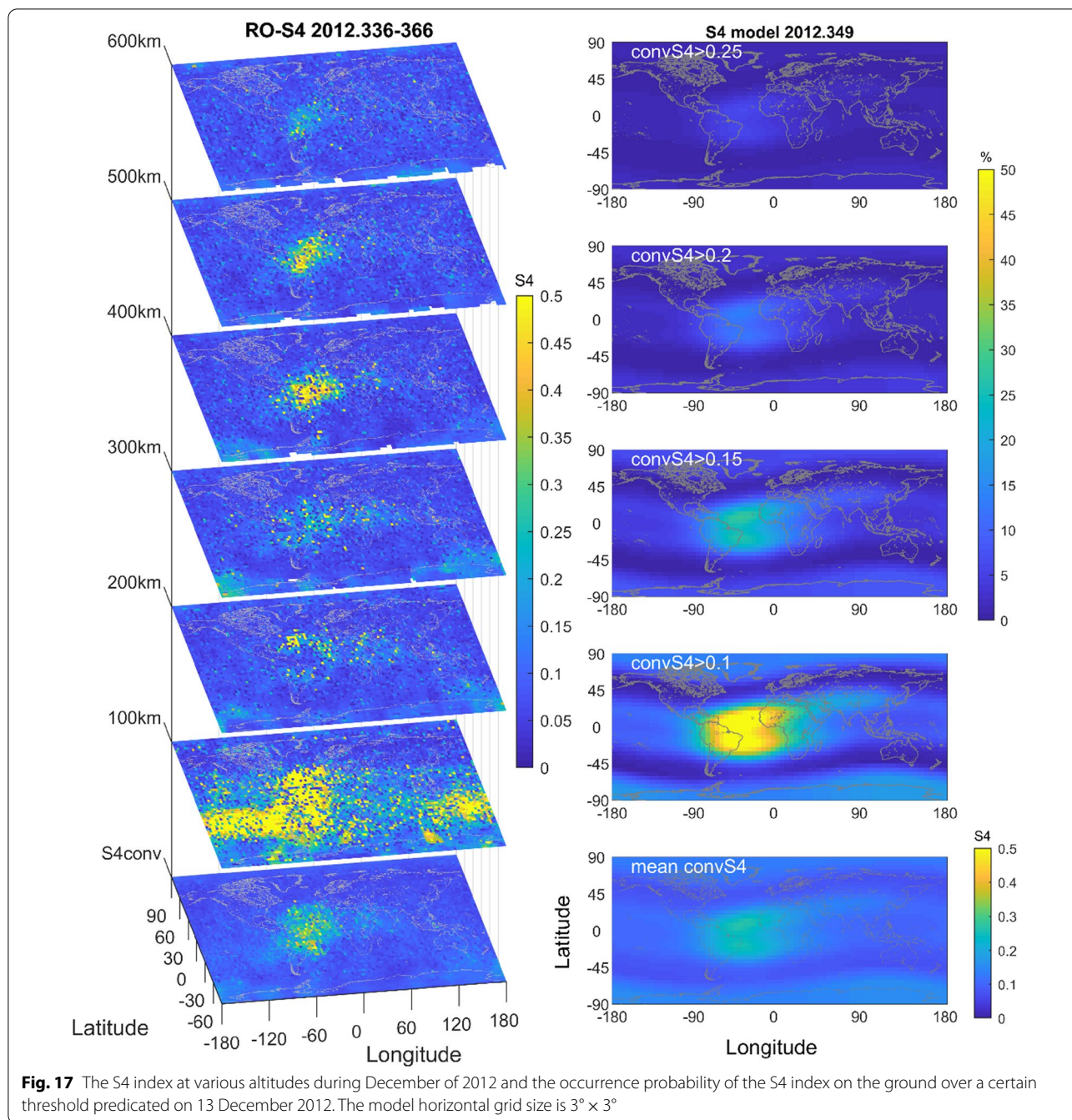
Such numerous observations following the launch of F3/C also led to the efforts towards developing scintillation forecast model. For practical ground-based applications, such as navigation, aviation communication etc., it is essential to know the net integrated impact, whereas F3/C provide S4 index encountered along the ray path in terms of tangent locations. Liu et al. (2016b) developed a method for integrating the distributed F3/C S4max in the ionosphere vertically to an equivalent quantity at the ground in a worst-case scenario. Yeh et al. (2020) conducted numerical analyses and confirmed that the scintillation is linearly proportional to the irregularity

amount along the ray path. Chen et al. (2017a, b) applied the method developed by Liu et al. (2016b) to construct a global empirical model of S4, which is termed F3CGS4 (F3/C global S4). F3CGS4 provides the climatological median S4-index of a designated year and day of year, for a given local time and location, requiring the corresponding solar activity F10.7 index as input. The F3CGS4 model have been updated recently by Chen et al. (2021b) by using the whole S4-index profile data and constructed the first global probability model for the S4-index of L-band scintillations.

Figure 17 displays the S4 index at various altitudes during December of 2012 and the different thresholds of the S4 index observing on the ground on 13 December 2012. Owing to the sporadic Es layer (e.g., Yeh et al. 2014), the S4 index becomes most intense at about 100 km altitude in approximately 30°S latitude. The intense probabilities frequently occur between South America and East Africa sectors. Moreover, based on Chen et al. (2021b), Liu and Wu (2021), for the first time, report the month-longitude distribution of ROTI (Rate Of Tec Index) in the equatorial/low latitude ionosphere in various years. Such advances based on the F3/C measurements reveal the potential for further improvements in the scintillation forecast models with more measurements, and eventually achieving global scintillation monitoring capabilities. The next section briefly examines how the follow-up mission for F3/C could play further role towards realizing these goals.

4 F7/C2 ionospheric progresses

The F7/C2 constellation was originally planned to be comprising of a first launch of six satellites with 24° inclination and 550 km altitude and a second launch of six satellites with 72° inclination and 800 km altitude, together with a wind-hunter satellite (hereafter named, TRITON or F7R) at >24° inclination and 500–600 km altitude, observing the sea surface's wind. This configuration would have enhanced the observations in the equatorial region over what was collected with the F3/C. Science payloads of IVM and RFB onboard the first launch satellites were provided by the US side, while those onboard the second launch satellites were to be furnished by the Taiwanese side. TRITON was designed and manufactured by NSPO. According to NSPO (<https://www.nspo.narl.org.tw>), TRITON consists of a 300-kg satellite equipped with a GNSS-Reflectometry (GNSS-R) payload to collect GNSS signals reflected by the Earth's surface from a low Earth orbit. The retrieved signals could be used to examine soil characteristics, understand air-sea interactions, and in the applications for predicting typhoon intensity. The measurements could be used to derive sea wave height and sea surface wind speed, which



are essential to conduct research on typhoon intensity and path prediction.

4.1 Advances and limitations

Since only the first launch was carried out, six small satellites of F7/C2 travel on their mission orbits at 550 km altitude with an inclination angle of 24 degrees, which results in TGRS observing more than 4000 electron density profiles per day between about 50-deg north and

south latitudes; IVM measuring the temperature, density, and velocity of ions within 24-deg latitudes; and RFB topographically scanning the electron density and scintillation within 45-deg latitudes. These allow us intensively study plasma structures and dynamics as well as accurately observing ionospheric weather in the equatorial/low-/middle-latitude ionosphere. One of the advantages of having the F7/C2 orbit at 550 km altitude is that while TGRS observes the 3D electron density structures, IVM

provides a better understanding of the associated dynamics. Figure 18 displays that TGRS and IVM data during the daytime at 1500 LT and nighttime at 0300 LT in September 2019. During the daytime, prominent co-located WN4 signatures appear in the TGRS electron density at 300, 400, and 500 km altitude as well as in the IVM ion density and ion temperature at the satellite altitude of 550 km. The agreement between TGRS electron density and IVM ion density meets the plasma characteristics of quasi-neutrality (Kelley 2009), while the opposite polarity of increase/decrease between ion density and ion temperature might be due to the cooling process via the Coulomb collision (Bilitza 1975). Although not yet being examined in detail, the ion velocity might shed some light on the formation mechanisms of WN4. By contrast, during the nighttime, four prominent PDB features in the TGRS electron density prominently appear at 200–500 km altitude and in the IVM ion density and ion temperature at 550 km altitude. Apart from the one North PDB and three South PDBs appearing in solstice months reported by Chang et al. (2020), the four PDBs

concurrently appearing in the equinox month of September 2019 in Fig. 18 suggest that further investigations are necessary to understand more details about these plasma structures. Thus, to uncover the cuneal mechanisms of PDBs, the IVM ion velocity could again play an important role. Moreover, TGRS and IVM concurrent observations will provide more details on the EIA formation owing to the photoionization, ion composition, plasma fountain, and neutral wind effects.

The other advantage of having the F7/C2 orbit at 550 km altitude is that IVM probes plasma irregularities while TGRS sounds ionospheric scintillations. Figure 19 illustrates the month-longitude distribution of irregularities from the deviation of IVM ion density and the S4 index of GPS L-band scintillations on the ground (see Liu et al. 2016b) and at various altitudes within ± 15 -deg magnetic latitudes in the nighttime of 2020. The deviation of IVM density refers to the average difference of the electron density over $\pm 15^\circ$ magnetic latitudes within a longitude bin of 2.5° from the corresponding median value for each month (e.g., Huang et al. 2014). Only

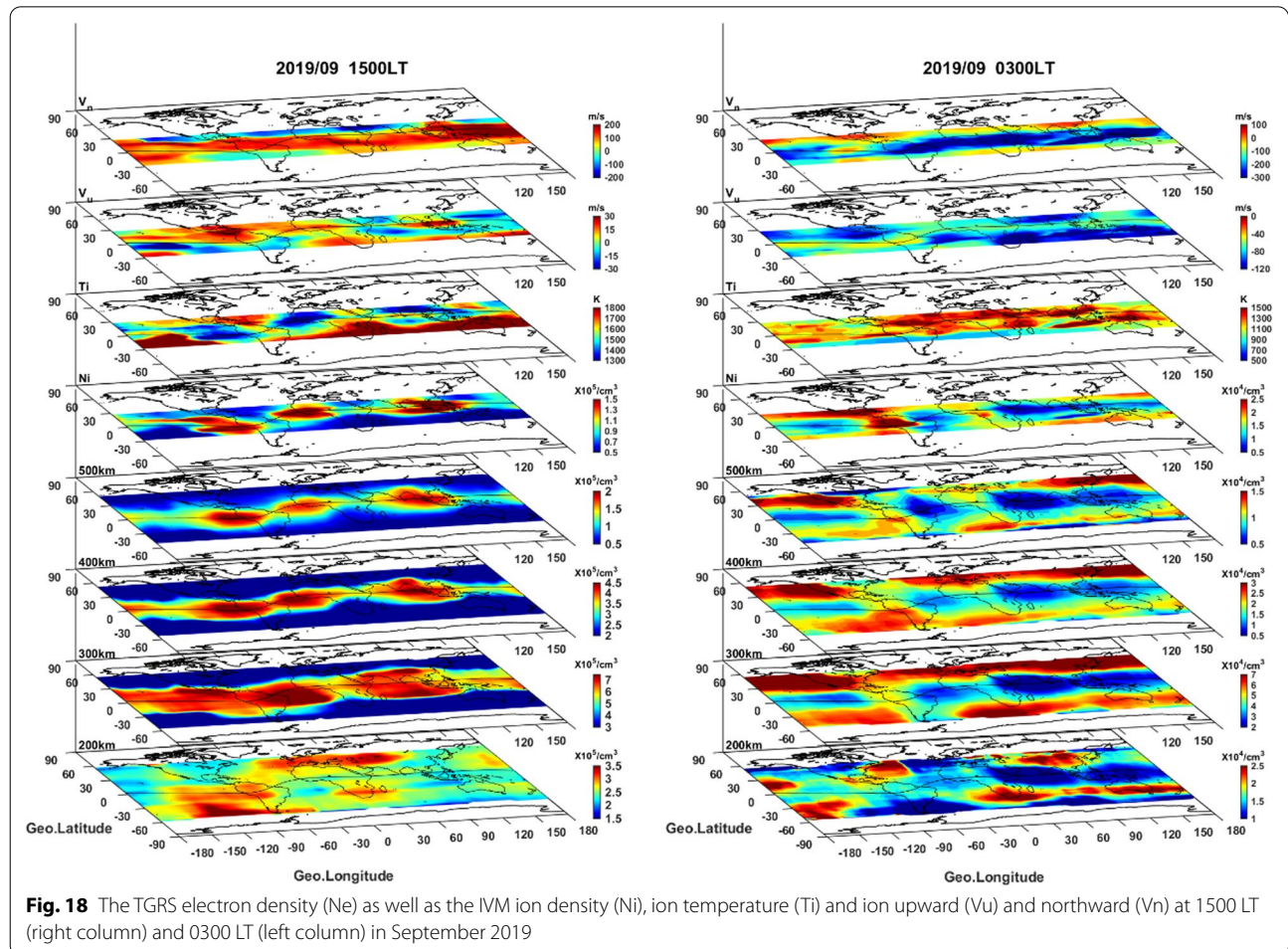


Fig. 18 The TGRS electron density (Ne) as well as the IVM ion density (Ni), ion temperature (Ti) and ion upward (Vu) and northward (Vn) at 1500 LT (right column) and 0300 LT (left column) in September 2019

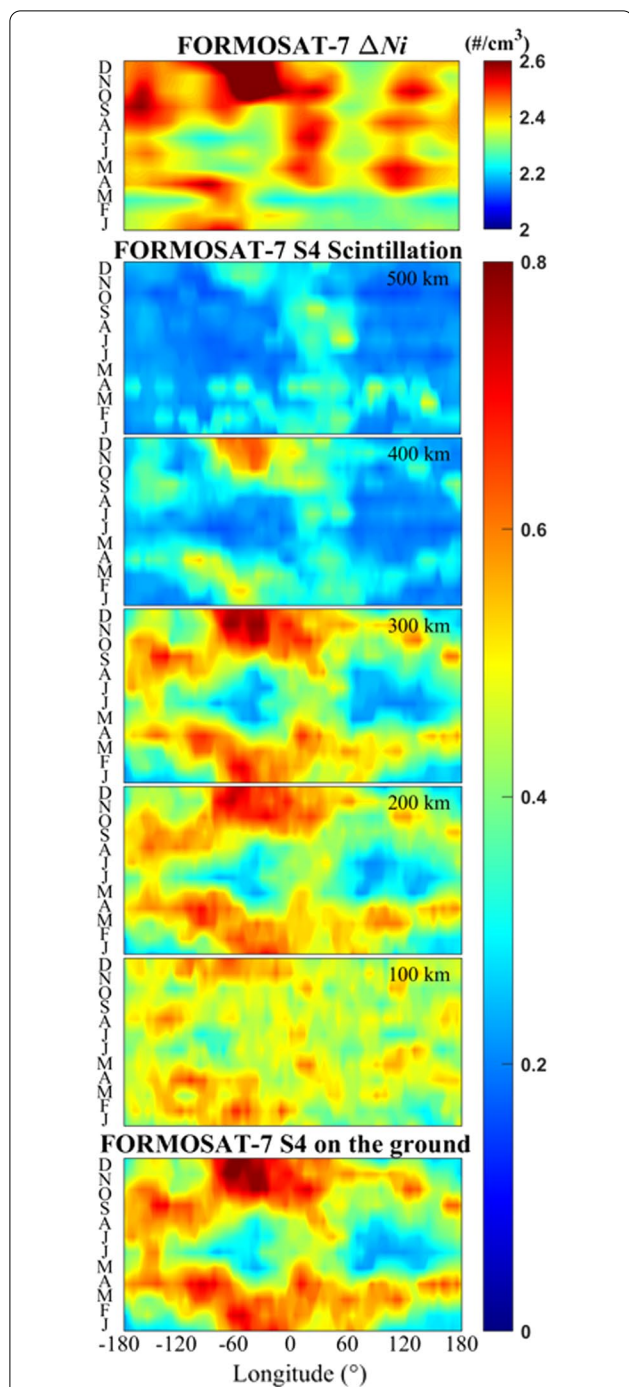


Fig. 19 The month-longitude distribution of F7/C2 IVM and TGRS observations within ± 15 -deg magnetic latitude during the nighttime of 2000–0000 LT in 2020. The IVM deviation ion density (ΔNi , top panel) and the S4 scintillation index at 500, 400, 300, 200, and 100 km altitude and on the ground (bottom panel)

those satellites that are near the final mission orbits are used. The month-longitude distribution of the S4 index at various altitudes are nearly identical, which shows

two low-/free-scintillation zones centered around $- 50^\circ$ and $120^\circ E$ during March–September of 2020, especially at 300 km altitude and on the ground. This suggests that the scintillation observed on the ground is proportional to the S4 over the altitudes of largest ambient electron density around the F2-peak. Huang et al. (2022) recently applied the F7/C2 IVM measurements to examine the irregularity distribution and highlighted the influence of background ion-density, especially in low solar activity conditions.

The global S4 pattern revealed in Fig. 19 in different seasons generally agree well with those reported earlier (e.g. Gentile et al. 2006), and indicate that evening plasma updrift is crucial in the irregularity occurrence (e.g., Retterer and Gentile 2009). On the other hand, the distribution of the deviation of IVM ion density seems not well agree with that of the TGRS S4 index observed in the ionosphere and on the ground, especially $60\text{--}180^\circ E$. This might be due to that the overall irregularity growth rate and the subsequent evolution to the topside would be rather diminished during the low solar activity year of 2020. Moreover, S4 is mainly influenced by the irregularities at the tangent region whereas IVM responds to the variations at the satellite location. Nevertheless, the IVM ion density and the TGRS S4 shall be able to successfully monitor ionospheric irregularities and scintillations as the next solar maximum is approaching.

Without the second launch of six satellites, F7/C2 observations do not cover the middle- and high-latitude ionosphere. Lin et al. (2017) conducted an OSSE study of ionospheric weather nowcast (i.e., GIS) by assimilating the TEC observed from ground-based GPS receivers and space-based F3/C GOX and F7/C2 TGRS into the IRI model. The F7/C2 plus GPS OSSE results illustrated that assimilating the F7/C2 first launch data can help reconstruct detailed structures of EIA but yields relatively poor results in the middle- and high-latitude regions due to the data coverage of the F7/C2 first launch. By contrast, assimilating F7/C2 both first and second launch data yields the best ionospheric specification not only at low latitude but at all latitudes. Therefore, it is vitally important to have a high inclination constellation for the global coverage.

4.2 Prospect of ionospheric observation

GPS radio occultations for the first time provide global and uniform observations for the 3D ionospheric plasma structures and dynamics. F3/C GOX allows scientists studying and uncovering causal physics mechanisms of EIA and WN4 in the equatorial/low latitude; the middle latitude trough (plasmopause) and OSA in the middle latitude; and WSA and the aurora oval in the high latitude ionosphere. F3/C also enabled finding

new features of plasma cave/tunnel, PDB; observing ionospheric disturbances triggered by seismic waves and tsunamis; and detecting signatures of the lithosphere–atmosphere–ionosphere coupling. The most significant impact is that F3/C has made it possible to routinely conduct ionospheric weather monitoring, nowcasting, and forecasting.

The information of ionospheric weather including various electron density structures discovered by the F3/C and F7/C2 as well as the density irregularities resulting from plasma instabilities have practical applications, for example the ground-based augmentation system (GBAS). GBAS is a system based on measurements by multiple ground reference GNSS receivers usually sitting at or near an airport to provide corrections and integrity information for GNSS signals, and navigation guidance for precision approach and landing for civil aviation (Saito et al. 2017). As the ionospheric delays are among the sources of total range errors of GBAS, the effect of inhomogeneities of the ionosphere (or spatial gradient) is an important issue for the GBAS applications. Knowing the spatial gradient of the ionosphere and its variations will be useful to implement the GBAS application and availability. The requirements of GBAS Landing System are defined by the International Civil Aviation Organization (ICAO). The electron density irregularities resulting in scintillation of GNSS signals is also crucial to the GBAS since the strong phase scintillations could stress phase lock loops (PLL) in GPS/GNSS receivers and result in loss of phase lock and frequent cycle slips (Humphreys et al. 2010). As a result, knowledge of the effect at the low latitude ionosphere would be important to assess the performance of GNSS for the aeronautical approach with vertical guidance (APV) performance requirements as specified by the ICAO (Roy and Paul 2013).

In addition to such possible practical applications providing support for GBAS and other performance requirements by ICAO, the prospect of F7/C2 includes the TGRS observing ionospheric EIA, plasma cave, WN4, PDB, etc. in detail and thus significantly improving ionospheric weather forecast in the equatorial/low latitude ionosphere. The crucial role of F7/C2 IVM is to help uncover the physical mechanisms associated with the equatorial/low latitude signatures, monitoring ion temperatures and velocities (or electric fields); and can be injected into assimilation models to enhance the accuracy of the ionospheric weather forecast. In summary, to accomplish the F7/C2 mission, a high inclination constellation of six or more satellites with RO and in situ plasma payloads will be essential for ionospheric science explorations and ionospheric weather forecast, which shall have significant impacts on positioning, navigation, and communication applications.

Acknowledgements

Data of FORMOSAT-3/COSMIC and FORMOSAT-7/COSMIC-2 are retrieved from Taiwan Analysis Center for COSMIC (TACC, <https://tacc.cwb.gov.tw/v2/download.html>). All the figures are newly plotted by the authors, except Figs. 2, 5, and 20. The authors wish to thank JYL's graduate students, Ms. Mei-Yu Chen, Mr. Po-Han Lee and Mr. Chun-Yen Huang at Department of Space Science and Engineering, National Central University, Taiwan for graphing electron density structures of the EIA (Fig. 2), middle latitude trough (Fig. 5), and F7/C2 S4 index (Fig. 20), respectively. This study is supported by the Taiwan Ministry of Science and Technology grant MOST 108-2119-M-008-001. This work was financially supported by the Center for Astronautical Physics and Engineering (CAPE) from the Featured Area Research Center program within the framework of Higher Education Sprout Project by the Ministry of Education (MOE) in Taiwan.

Author details

¹Center for Astronautical Physics and Engineering, National Central University, Taoyuan City, Taiwan. ²Department of Space Science and Engineer, National Central University, Taoyuan City, Taiwan. ³Center for Space and Remote Sensing Research, National Central University, Taoyuan City, Taiwan. ⁴Department of Earth Sciences, National Cheng Kung University, Tainan City, Taiwan. ⁵Space Weather Operation Office, Center Weather Bureau, Taoyuan City, Taiwan. ⁶Institute of Geophysics and Geomatics, China University of Geosciences, Wuhan, China. ⁷High Altitude Observatory, National Center for Atmospheric Research, Boulder, USA. ⁸Ann and H. J. Smead Aerospace Engineering Sciences, University of Colorado, Boulder, USA.

Received: 28 January 2022 Accepted: 23 June 2022

Published online: 15 July 2022

References

- Anderson DN, Redmon RJ (2017) Forecasting scintillation activity and equatorial spread F. *Space Weather* 15:495–502. <https://doi.org/10.1002/2016SW001554>
- Anthes R, Bernhardt P, Cucurull L, Dymond K, Ector D, Healy S, Ho SP, Hunt D, Kuo Y, Manning K, McCormick C (2008) The COSMIC/Formosat-3 mission: early results. *Bull Am Meteorol Soc* 89:313–333. <https://doi.org/10.1175/BAMS-89-3-313>
- Appleton EV, Naismith R (1935) Some further measurements of upper atmospheric ionization. *Proc R Soc Lond A* 150:685–708. <https://doi.org/10.1098/rspa.1935.0129>
- Arras C, Wickert J (2018) Estimation of ionospheric sporadic E intensities from GPS radio occultation measurements. *J Atmos Solar Terr Phys* 47:60–63. <https://doi.org/10.1016/j.jastp.2017.08.006>
- Arras C, Wickert J, Beyerle G, Heise S, Schmidt T, Jacobi C (2008) A global climatology of ionospheric irregularities derived from GPS radio occultation. *Geophys Res Lett* 35:L14809. <https://doi.org/10.1029/2008GL034158>
- Arras C, Jacobi C, Wickert J (2009) Semidiurnal tidal signature in sporadic E occurrence rates derived from GPS radio occultation measurements at higher midlatitudes. *Ann Geophys* 27:2555–2563. <https://doi.org/10.5194/angeo-27-2555-2009>
- Baker DN, Daly E, Daglis I, Kappenman JG, Panasyuk M (2004) Effects of space weather on technology infrastructure. *Space Weather*. <https://doi.org/10.1029/2003SW000044>
- Bellchambers W, Piggott W (1958) Ionospheric measurements made at Halley Bay. *Nature* 182:1596–1597. <https://doi.org/10.1038/1821596a0>
- Bilitza D (1975) Models for the relationship between electron density and temperature in the upper ionosphere. *J Atmos Terr Phys* 37:1219–1222. [https://doi.org/10.1016/0021-9169\(75\)90193-2](https://doi.org/10.1016/0021-9169(75)90193-2)
- Boteler DH (2001) Space weather effects on power systems. In: Song P, Singer HJ, Siscoe GL (eds) *Space weather*, vol 125. American Geophysical Union. <https://doi.org/10.1029/GM125p0347>
- Brahmanandam PS, Uma G, Liu JY, Chu YH, Latha Devi NSMP, Kakinami Y (2012) Global S4 index variations observed using FORMOSAT-3/COSMIC GPS RO technique during a solar minimum year. *J Geophys Res* 117:A09322. <https://doi.org/10.1029/2012JA017966>
- Chang LC, Lin C-H, Yue J, Liu J-Y, Lin J-T (2013a) Stationary planetary wave and nonmigrating tidal signatures in ionospheric wave 3 and wave 4

- variations in 2007–2011 FORMOSAT-3/COSMIC observations. *J Geophys Res Space Physics* 118:6651–6665. <https://doi.org/10.1002/jgra.50583>
- Chang LC, Lin C-H, Liu J-Y, Balan N, Yue J, Lin J-T (2013b) Seasonal and local time variation of ionospheric migrating tides in 2007–2011 FORMOSAT-3/COSMIC and TIE-GCM total electron content. *J Geophys Res Space Physics* 118:2545–2564. <https://doi.org/10.1002/jgra.50268>
- Chang FY, Liu JY, Chang LC, Lin CH, Chen CH (2015) Three-dimensional electron density along the WSA and MSNA latitudes probed by FORMOSAT-3/COSMIC. *Earth Planet Space* 67:156. <https://doi.org/10.1186/s40623-015-0326-8>
- Chang LC, Chiu P-Y, Salinas CCJH, Chen S-P, Duann Y, Liu J-Y et al (2018) On the relationship between E region scintillation and ENSO observed by FORMOSAT-3/COSMIC. *J Geophys Res Space Phys* 123:4053–4065. <https://doi.org/10.1029/2018JA025299>
- Chang FY, Liu JY, Fang TW, Rajesh PK, Lin CH (2020) Plasma depletion bays in the equatorial ionosphere observed by FORMOSAT-3/COSMIC during 2007–2014. *J Geophys Res Space Phys* 125(9):1–11. <https://doi.org/10.1029/2019JA027501>
- Chen CH, Lin CH, Chang LC, Huba JD, Lin JT, Saito A, Liu JY (2013) Thermospheric tidal effects on the ionospheric midlatitude summer nighttime anomaly using SAMI3 and TIEGCM. *J Geophys Res Space Physics* 118(6):3836–3845. <https://doi.org/10.1002/jgra.50340>
- Chen Y-T, Lin CH, Chen CH, Liu JY, Huba JD, Chang LC, Liu H-L, Lin JT, Rajesh PK (2014) Theoretical study of the ionospheric plasma cave in the equatorial ionization anomaly region. *J Geophys Res Space Phys* 119:10324–10335. <https://doi.org/10.1002/2014JA020235>
- Chen CH, Lin CH, Matsuo T, Chen WH, Lee IT, Liu JY, Lin JT, Hsu CT (2016a) Ionospheric data assimilation with thermosphere-ionosphere-electrodynamics general circulation model and GPS-TEC during geomagnetic storm conditions. *J Geophys. Res.* 121:5708–5722. <https://doi.org/10.1002/2015JA021787>
- Chen CH, Lin CH, Liu JY, Matsuo T, Chen WH (2016b) Ionospheric data assimilation modeling of 2015 St. Patrick's Day geomagnetic storm. *J Geophys Res* 121:11549–11559. <https://doi.org/10.1002/2016JA023346>
- Chen CH, Lin CH, Liu JY, Matsuo T, Chen WH (2016c) The impact of FORMOSAT-5/AIP on the ionospheric space weather. *Terr Atmos Ocean Sci* 28:129–137. [https://doi.org/10.3319/TAO.2016.09.30.01\(EOF5\)](https://doi.org/10.3319/TAO.2016.09.30.01(EOF5))
- Chen CH, Lin CH, Chen W-H, Matsuo T (2017a) Modeling the ionospheric prereversal enhancement by using coupled thermosphere-ionosphere data assimilation. *Geophys Res Lett* 44:1652–1659. <https://doi.org/10.1002/2016GL071812>
- Chen SP, Billitz D, Liu JY, Caton R, Chang LC, Yeh WH (2017b) An empirical model of L-band scintillation S4 index constructed by using FORMOSAT-3/COSMIC data. *Adv Space Res* 60(5):1015–1028. <https://doi.org/10.1016/j.asr.2017.05.031>
- Chen CY, Liu TJY, Lee IT, Rothkaehl H, Przepiorka D, Chang LC et al (2018) The midlatitude trough and the plasmopause in the nighttime ionosphere simultaneously observed by DEMETER during 2006–2009. *J Geophys Res Space Phys* 123:5917–5932. <https://doi.org/10.1029/2017JA024840>
- Chen CH, Lin CH, Matsuo T (2019) Ionospheric responses to the 21 August 2017 solar eclipse by using data assimilation approach. *Prog Earth Planet Sci* 6:13. <https://doi.org/10.1186/s40645-019-0263-4>
- Chen SP, Lin CH, Rajesh PK, Liu JY, Eastes R, Chou MY, Choi JM (2021a) Near real-time global plasma irregularity monitoring by FORMOSAT-7/COSMIC-2. *J Geophys Res Space Phys*. 126:e2020JA028339. <https://doi.org/10.1029/2020JA028339>
- Chen SP, Liu JY, Lin CH, Yeh WH (2021b) A global model for the occurrence probability of L-band scintillation S4-index. *Terr Atmos Ocean Sci.* <https://doi.org/10.3319/TAO.2021.08.10.03>
- Cheng CZ, Kuo Y-H, Anthes RA, Wu L (2006) Satellite constellation monitors global and space weather. *Eos Am Geophys Union* 87(17):166
- Chou M-Y, Wu Q, Pedatella NM, Chorniak I, Schreiner WS, Braun J (2020) Climatology of the equatorial plasma bubbles captured by FORMOSAT-3/COSMIC. *J Geophys Res Space Phys.* <https://doi.org/10.1029/2019JA027680>
- Chu CH, Huang CY, Fong CJ, Chen SY, Chen YH, YehKuo WHYH (2021) Atmospheric remote sensing using global navigation satellite systems: from FORMOSAT-3/COSMIC to FORMOSAT-7/COSMIC-2. *Terr Atmos Ocean Sci.* <https://doi.org/10.3319/TAO.2021.11.15.02>
- Chua DH, Dymond KF, Budzien SA, Coker C, Liu JY (2009) Horizontal ionospheric electron density gradients observed by FORMOSAT-3/COSMIC TIP: spatial distributions and effects on VLF wave propagation at mid-latitudes. *Terr Atmos Ocean Sci* 20:251–259. [https://doi.org/10.3319/TAO.2008.01.16.01\(F3C\)](https://doi.org/10.3319/TAO.2008.01.16.01(F3C))
- Coker C, Dymond KF, Budzien SA, Chua DH, Liu JY, Anderson DN, Basu S, Pedersen TR (2009) Observations of the ionosphere using the tiny ionospheric photometer. *Terr Atmos Ocean Sci.* 20:227–235. [https://doi.org/10.3319/TAO.2008.01.18.02\(F3C\)](https://doi.org/10.3319/TAO.2008.01.18.02(F3C))
- Davies K (1990) Ionospheric radio. Peter Peregrinus Ltd, London, p 580
- Dymond KF, Budzien SA, Chua DH, Coker C, Liu JY (2009) Tomographic reconstruction of the low-latitude night time electron density using FORMOSAT-3/COSMIC radio occultation and UV photometer data. *Terr Atmos Ocean Sci* 20:215–226. [https://doi.org/10.3319/TAO.2008.01.15.01\(F3C\)](https://doi.org/10.3319/TAO.2008.01.15.01(F3C))
- England SL, Immel TJ, Sagawa E, Henderson SB, Hagan ME, Mende SB, Frey HU, Swenson CM, Paxton LJ (2006) Effect of atmospheric tides on the morphology of the quiet time, postsunset equatorial ionospheric anomaly. *J Geophys. Res.* 111:A10S19. <https://doi.org/10.1029/2006JA011795>
- Forbes JM, Russell J, Miyahara S, Zhang X, Palo S, Mlynarczyk M, Mertens CJ, Hagan ME (2006) Troposphere-thermosphere tidal coupling as measured by the SABER instrument on TIMED during July–September 2002. *J Geophys. Res.* 111:A10S06. <https://doi.org/10.1029/2005JA011492>
- Gentile LC, Burke WJ, Rich FJ (2006) A climatology of equatorial plasma bubbles from DMSP 1989–2004. *Radio Sci* 41:RS521. <https://doi.org/10.1029/2005RS003340>
- Goncharenko L, Zhang S-R (2008) Ionospheric signatures of sudden stratospheric warming: ion temperature at middle latitude. *Geophys Res Lett* 35:L21103. <https://doi.org/10.1029/2008GL035684>
- Goncharenko LP, Chau JL, Liu H-L, Coster AJ (2010a) Unexpected connections between the stratosphere and ionosphere. *Geophys Res Lett* 37:L10101. <https://doi.org/10.1029/2010GL043125>
- Goncharenko LP, Coster AJ, Chau JL, Valladares CE (2010b) Impact of sudden stratospheric warmings on equatorial ionization anomaly. *J Geophys. Res.* 115:A00G07. <https://doi.org/10.1029/2010JA015400>
- Hajji GA, Wilson BD, Wang C, Pi X, Rosen IG (2004) Data assimilation of ground GPS total electron content into a physics-based ionospheric model by use of the Kalman filter. *Radio Sci* 39:RS1505. <https://doi.org/10.1029/2002RS002859>
- Heelis MH, Howe BM (2004) Global Assimilation of ionospheric measurements (GAIM). *Radio Sci* 39:RS1502. <https://doi.org/10.1029/2002RS002794>
- Hsiao TY, Tsai LC, Liu CH (2009) The initial results from the LITN of the FORMOSAT-3 TBB program. *Terr Atmos Ocean Sci* 20:261–271. [https://doi.org/10.3319/TAO.2007.12.03.01\(F3C\)](https://doi.org/10.3319/TAO.2007.12.03.01(F3C))
- Hsu ML, Rajesh PK, Liu JY, Tsai LC, Tsai HF, Lin CH, Dymond KF, Coker C, Chua DH, Budzien SA, Cheng CZ (2009) Ionospheric electron density concurrently derived by TIP and GOX of FORMOSAT-3/COSMIC. *Terr Atmos Ocean Sci* 20:207–214. [https://doi.org/10.3319/TAO.2008.04.24.02\(F3C\)](https://doi.org/10.3319/TAO.2008.04.24.02(F3C))
- Hsu C-T, Matsuo T, Wang W, Liu J-Y (2014) Effects of inferring unobserved thermospheric and ionospheric state variables by using an Ensemble Kalman Filter on global ionospheric specification and forecasting. *J Geophys Res Space Phys* 119:9256–9267. <https://doi.org/10.1002/2014JA020390>
- Hsu C-T, Matsuo T, Yue X, Fang T-W, Fuller-Rowell T, Ide K, Liu J-Y (2018a) Assessment of the impact of FORMOSAT-7/COSMIC-2 GNSS RO observations on midlatitude and low-latitude ionosphere specification: observing system simulation experiments using ensemble square root filter. *J Geophys Res Space Phys* 123:2296–2314. <https://doi.org/10.1002/2017JA025109>
- Hsu C-T, Matsuo T, Liu J-Y (2018b) Impact of assimilating the FORMOSAT3/COSMIC and FORMOSAT-7/COSMIC-2 RO data on the midlatitude and low-latitude ionospheric specification. *Earth Space Sci* 5:875–890. <https://doi.org/10.1029/2018EA000447>
- Huang C-S, de La Beaujardiere O, Roddy PA, Hunton DE, Liu JY, Chen SP (2014) Occurrence probability and amplitude of equatorial ionospheric irregularities associated with plasma bubbles during low and moderate solar activities (2008–2012). *J Geophys Res Space Phys* 119:1186–1199. <https://doi.org/10.1002/2013JA019212>
- Huang C-Y, Liu J-Y, Chang F-Y, Lin C-Y, Chao C-K, Chang LC, Lin CY (2022) Instantaneous amplitude of low-latitude ionospheric irregularities probed by ROCSAT-1, DEMETER, and FORMOSAT-7/COSMIC-2. *Adv Space Res.* <https://doi.org/10.1016/j.asr.2022.05.024>

- Huba JD, Joyce G (2010) Global modeling of equatorial plasma bubbles. *Geophys Res Lett* 37:L17104. <https://doi.org/10.1029/2010GL044281>
- Humphreys TE, Psiaki ML, Kintner PM Jr (2010) Modelling the effects of ionospheric scintillation on GPS carrier phase tracking. *IEEE Trans Aerosp Electron Syst* 46(4):1624–1637
- Immel TJ, Sagawa E, England SL, Henderson SB, Hagan ME, Mende SB, Frey HU, Swenson CM, Paxton LJ (2006) Control of equatorial ionospheric morphology by atmospheric tides. *Geophys Res Lett* 33:L15108. <https://doi.org/10.1029/2006GL026161>
- Jin H, Miyoshi Y, Pancheva D, Mukhtarov P, Fujiwara H, Shinagawa H (2012) Response of migrating tides to the stratospheric sudden warming in 2009 and their effects on the ionosphere studied by a whole atmosphere-ionosphere model GAIA with COSMIC and TIMED/SABER observations. *J Geophys Res* 117:A10323. <https://doi.org/10.1029/2012JA017650>
- Kalman RE (1960) A new approach to linear filtering and prediction problems. *J Basic Eng* 82(1):35–45. <https://doi.org/10.1115/1.3662552>
- Kalman RE, Bucy R (1961) New results in linear filtering and prediction theory. *J Basic Eng* 83(1):95–108. <https://doi.org/10.1115/1.3658902>
- Kelley M (2009) *The Earth's ionosphere: plasma physics and electrodynamics*, 2nd edn. Academic Press, San Diego, Calif
- Kepkar A, Arras C, Wickert J, Schuh H, Alizadeh M, Tsai L-C (2020) Occurrence climatology of equatorial plasma bubbles derived using FormoSat-3 / COSMIC GPS radio occultation data. *Ann Geophys* 38:611–623. <https://doi.org/10.5194/angeo-38-611-2020>
- Ko CP, Yeh HC (2010) COSMIC/FORMOSAT-3 observations of equatorial F region irregularities in the SAA longitude sector. *J Geophys Res* 115:A11309. <https://doi.org/10.1029/2010JA015618>
- Lanzerotti LJ (2001) Space weather effects on technologies. In: Song P, Singer HJ, Siscoe GL (eds) *Space weather*. <https://doi.org/10.1029/GM125p0011>
- Lee IT, Wang W, Liu JY, Chen CY, Lin CH (2011) The ionospheric midlatitude trough observed by FORMOSAT-3/COSMIC during solar minimum. *J Geophys Res* 116:A06311. <https://doi.org/10.1029/2010JA015544>
- Lee IT, Liu JY, Lin CH, Oyama K-I, Chen CY, Chen CH (2012a) Ionospheric plasma caves under the equatorial ionization anomaly. *J Geophys Res* 117:A11309. <https://doi.org/10.1029/2012JA017868>
- Lee IT, Matsuo T, Richmond AD, Liu JY, Wang W, Lin CH et al (2012b) Assimilation of FORMOSAT-3/COSMIC electron density profiles into a coupled thermosphere/ionosphere model using ensemble Kalman filtering. *J Geophys Res* 117:A10318. <https://doi.org/10.1029/2012JA017700>
- Lee IT, Tsai HF, Liu JY, Lin CH, Matsuo T, Chang LC (2013) Modeling impact of FORMOSAT-7/COSMIC-2 mission on ionospheric space weather monitoring. *J Geophys Res Space Phys* 118:6518–6523. <https://doi.org/10.1002/jgra.50538>
- Lin CH, Liu JY, Fang TW, Chang PY, Tsai HF, Chen CH, Hsiao CC (2007a) Motions of the equatorial ionization anomaly crests imaged by FORMOSAT-3/COSMIC. *Geophys Res Lett* 34:L19101. <https://doi.org/10.1029/2007GL030741>
- Lin CH, Wang W, Hagan ME, Hsiao CC, Immel TJ, Hsu ML, Liu JY, Paxton LJ, Fang TW, Liu CH (2007b) Plausible effect of atmospheric tides on the equatorial ionosphere observed by the FORMOSAT-3/COSMIC: three-dimensional electron density structures. *Geophys Res Lett* 34:L11112. <https://doi.org/10.1029/2007GL029265>
- Lin CH, Hsiao CC, Liu JY, Liu CH (2007c) Longitudinal structure of the equatorial ionosphere: time evolution of the four-peaked EIA structure. *J Geophys Res* 112:A12305. <https://doi.org/10.1029/2007JA012455>
- Lin CH, Liu JY, Cheng CZ, Chen CH, Liu CH, Wang W, Burns AG (2009) Three-dimensional ionospheric electron density structure of the Weddell Sea anomaly. *J Geophys Res* 114:A02312. <https://doi.org/10.1029/2008JA013455>
- Lin CH, Liu CH, Liu JY, Chen CH, Burns AG, Wang W (2010) Midlatitude summer nighttime anomaly of the ionospheric electron density observed by FORMOSAT-3/COSMIC. *J Geophys Res* 115:A03308. <https://doi.org/10.1029/2009JA014084>
- Lin CH, Lin JT, Chang LC, Liu JY, Chen CH, Chen WH, Huang HH, Liu CH (2012a) Observations of global ionospheric responses to the 2009 stratospheric sudden warming event by FORMOSAT-3/COSMIC. *J Geophys Res Space Phys* 117:A06323. <https://doi.org/10.1029/2011JA017230>
- Lin JT, Lin CH, Chang LC, Huang HH, Liu JY, Chen AB, Chen CH, Liu CH (2012b) Observational evidence of ionospheric migrating tide modification during the 2009 stratospheric sudden warming. *Geophys Res Lett* 39:L02101. <https://doi.org/10.1029/2011GL050248>
- Lin CH, Lin JT, Chang LC, Chen WH, Chen CH, Liu JY (2013) Stratospheric sudden warming effect on the ionospheric migrating tides during 2008–2010 observed by FORMOSAT-3/COSMIC. *J Atmos Solar Terr Phys* 103(Special Issue):66–75. <https://doi.org/10.1016/j.jastp.2013.03.026>
- Lin CY, Matsuo T, Liu JY, Lin CH, Tsai HF, Araujo-Pradere EA (2015) Ionospheric assimilation of radio occultation and ground-based GPS data using non-stationary background model error covariance. *Atmos Meas Tech* 8:171–182. <https://doi.org/10.5194/amt-8-171-2015>
- Lin CY, Matsuo T, Liu JY, Lin CH, Huba JD, Tsai HF, Chen CY (2017) Data assimilation of ground-based GPS and radio occultation total electron content for global ionospheric specification. *J Geophys Res Space Phys* 122:10876–10886. <https://doi.org/10.1002/2017JA024185>
- Lin JT, Lin CH, Lin CY, Pedatella NM, Rajesh PK, Matsuo T, Liu JY (2019) Revisiting the modulations of ionospheric solar and lunar migrating tides during the 2009 stratospheric sudden warming by using global ionosphere specification. *Space Weather* 17:767–777. <https://doi.org/10.1029/2019SW002184>
- Lin JT, Lin CH, Rajesh PK, Yue J, Lin CY, Matsuo T (2020a) Local-time and vertical characteristics of quasi-6-day oscillation in the ionosphere during the 2019b Antarctic Sudden Stratospheric Warming. *Geophys Res Lett* 47:e2020GL090345. <https://doi.org/10.1029/2020GL090345>
- Lin C-Y, Lin CC-H, Liu J-Y, Rajesh PK, Matsuo T, Chou M-Y et al (2020b) The early results and validation of FORMOSAT-7/COSMIC-2 space weather products: global ionospheric specification and Ne-aided Abel electron density profile. *J Geophys Res Space Phys* 125:e2020JA028028. <https://doi.org/10.1029/2020JA028028>
- Liu JY (2019) Ionospheric GNSS radio occultation observations of FORMOSAT-3/COSMIC and FORMOSAT-7/COSMIC. 20th International Beacon Satellite Symposium, Mazury and Olsztyn, 19–23 August 2019
- Liu JY, Wu SA (2021) Global observations of ROTI by using ground-based GNSS receivers. *Terr Atmos Ocean Sci*. <https://doi.org/10.3319/TAO.2021.07.26.03>
- Liu JY, Tsai YB, Ma KF, Chen YI, Tsai HF, Lin CH, Kamogawa M, Lee CP (2006) Ionospheric GPS total electron content (TEC) disturbances triggered by the 26 December 2004 Indian Ocean tsunami. *J Geophys Res* 111:A05303. <https://doi.org/10.1029/2005JA011200>
- Liu JY, Chen YI, Chen CH, Liu CY, Chen CY, Nishihashi M, Li JZ, Xia YQ, Oyama KI, Hattori K, Lin CH (2009) Seismo-ionospheric GNSS GPS total electron content anomalies observed before the 12 May 2008 Mw7.9 Wenchuan earthquake. *J Geophys. Res.* 114:A04320. <https://doi.org/10.1029/2008JA013698>
- Liu JY, Lin CY, Lin CH, Tsai HF, Solomon SC, Sun YY, Lee IT, Schreiner WS, Kuo YH (2010a) Artificial plasma cave in the low-latitude ionosphere results from the radio occultation inversion of the FORMOSAT-3/COSMIC. *J Geophys Res* 115:A07319. <https://doi.org/10.1029/2009JA015079>
- Liu JY, Tsai HF, Lin CH, Kamogawa M, Chen YI, Lin CH, Huang BS, Yu SB, Yeh YH (2010b) Coseismic ionospheric disturbances triggered by the Chi-Chi earthquake. *J Geophys Res* 115:A08303. <https://doi.org/10.1029/2009JA014943>
- Liu JY, Chen CH, Lin CH, Tsai HF, Chen CH, Kamogawa M (2011) Ionospheric disturbances triggered by the 11 March 2011 M9.0 Tohoku Earthquake. *J Geophys Res* 116:A06319. <https://doi.org/10.1029/2011JA016761>
- Liu JY, Loren CW, Chang CK, Chao MQ, Chen YH, Chu LN, Hau CM, Huang CL, Kuo LC, Lee LH, Lyu CH, Lin CJ, Pan JH, Shue CLS, Tsai LC, Yang YH, Lin CH, Hsu RR, Su HT (2016a) The fast development of solar terrestrial sciences in Taiwan. *Geosci Lett* 3(18):1–11. <https://doi.org/10.1186/s40562-016-0049-0>
- Liu JY, Chen SP, Yeh WH, Tsai HF, Rajesh PK (2016b) Worst-case GPS scintillations on the ground estimated from radio occultation observations of FORMOSAT-3/ COSMIC during 2007–2014. *Surv Geophys* 37:791–809. <https://doi.org/10.1007/s10712-015-9355-x>
- Liu JY, Chen CY, Sun YY, Lee IT, Chum J (2019) Fluctuations on vertical profiles of the ionospheric electron density perturbed by the March 11, 2011b M9.0 Tohoku earthquake and tsunami. *GPS Solut* 23(3):1–10. <https://doi.org/10.1007/s10291-019-0866-7>

- Liu JY, Chang FY, Lin CY, Chen YI, iSTEP group (2020a) Ionospheric earthquake precursors and space weather observed by FORMOSAT-7/COSMIC-2, abstract #NH005-02, American Geophysical Union, Fall Meeting 2020a
- Liu JY, Chang FY, Charles CH, Lin CY, Lin SP, Chen, Rajesh PK (2020b) Advances in low-latitude ionosphere observed by FORMOSAT-7/COSMIC-2, abstract #SA038-04, American Geophysical Union, Fall Meeting 2020b
- Liu JY, Lin CH, Rajesh PK, Lin CY, Chang FY, Lee IT, Fang TW, Fuller-Rowell D, Chen SP (2022) Advances in ionospheric space weather by using FORMOSAT-7/COSMIC-2 GNSS radio occultations. *Atmosphere* 13:858. <https://doi.org/10.3390/atmos13060858>
- Matsuo T, Araujo-Pradere EA (2011) Role of thermosphere-ionosphere coupling in a global ionospheric specification. *Radio Sci* 46:RS0D23. <https://doi.org/10.1029/2010RS004576>
- Matsuo T, Lee IT, Anderson JL (2013) Thermospheric mass density specification using an Ensemble Kalman Filter. *J Geophys Res Space Phys* 118:1–12. <https://doi.org/10.1002/jgra.50162>
- Oberheide J, Hagan ME, Roble RG (2003) Tidal signatures and aliasing in temperature data from slowly precessing satellites. *J Geophys Res* 108(A2):1055. <https://doi.org/10.1029/2002JA009585>
- Pancheva D, Mukhtarov P (2010) Strong evidence for the tidal control of the longitudinal structure of the ionospheric F-region. *Geophys Res Lett* 37:L14105. <https://doi.org/10.1029/2010GL044039>
- Pancheva D, Mukhtarov P (2011) Stratospheric warmings: the atmosphere-ionosphere coupling paradigm. *J Atmos Sol Terr Phys* 73:1697–1702. <https://doi.org/10.1016/j.jastp.2011.03.006>
- Pancheva D, Miyoshi Y, Mukhtarov P, Jin H, Shinagawa H, Fujiwara H (2012) Global response of the ionosphere to atmospheric tides forced from below: comparison between COSMIC measurements and simulations by atmosphere-ionosphere coupled model GAIA. *J Geophys Res* 117:A07319. <https://doi.org/10.1029/2011JA017452>
- Pedatella NM, Forbes JM (2010) Evidence for stratosphere sudden warming-ionosphere coupling due to vertically propagating tides. *Geophys Res Lett* 37:L11104. <https://doi.org/10.1029/2010GL043560>
- Pi X, Wang C, Hajj GA, Rosen G, Wilson BD, Bailey GJ (2003) Estimation of E × B drift using a global assimilative ionospheric model: an observation system simulation experiment. *J Geophys Res* 108(A2):1075. <https://doi.org/10.1029/2001JA009235>
- Qiu L, Yu T, Yan X, Sun Y-Y, Zuo X, Yang N et al (2021) Altitudinal and latitudinal variations in ionospheric sporadic-E layer obtained from FORMOSAT-3/COSMIC radio occultation. *J Geophys Res Space Phys* 126:e2021JA029454. <https://doi.org/10.1029/2021JA029454>
- Rajesh PK, Liu JY, Balan N, Lin CH, Sun YY, Pulinet SA (2016) Morphology of midlatitude electron density enhancement using total electron content measurements. *J Geophys Res Space Phys* 121:1503–1517. <https://doi.org/10.1002/2015JA022251>
- Rajesh PK, Lin CH, Lin CY, Chen CH, Liu JY, Matsuo T et al (2021a) Extreme positive ionosphere storm triggered by a minor magnetic storm in deep solar minimum revealed by FORMOSAT-7/COSMIC-2 and GNSS observations. *J Geophys Res Space Phys* 126:e2020JA028261. <https://doi.org/10.1029/2020JA028261>
- Rajesh PK, Lin CH, Lin JT, Lin CY, Yue J, Matsuo T, Chen SP, Chen CH (2021b) Day-to-day variability of ionosphere electron density during solar minimum derived from FORMOSAT-7/COSMIC-2 measurements. *Terr Atmos Ocean Sci*. <https://doi.org/10.3319/TAO.2021.08.01.01>
- Ratcliffe JA (1972) An introduction to the ionosphere and magnetosphere, vol 256. Cambridge University Press, New York
- Retterer JM, Gentile LC (2009) Modeling the climatology of equatorial plasma bubbles observed by DMSF. *Radio Sci* 44:RS0A31. <https://doi.org/10.1029/2008RS004057>
- Rishbeth H (2000) The equatorial F-layer: progress and puzzles. *Ann Geophys* 18:730. <https://doi.org/10.1007/s00585-000-0730-6>
- Roy B, Paul A (2013) Impact of space weather events on satellite-based navigation. *Space Weather* 11:680–686. <https://doi.org/10.1002/2013SW001011>
- Sagawa E, Immel TJ, Frey HU, Mende SB (2005) Longitudinal structure of the equatorial anomaly in the nighttime ionosphere observed by IMAGE/FUV. *J Geophys Res* 110:A11302. <https://doi.org/10.1029/2004JA010848>
- Saito S, Sunda S, Lee J et al (2017) Ionospheric delay gradient model for GBAS in the Asia-Pacific region. *GPS Solut* 21:1937–1947. <https://doi.org/10.1007/s10291-017-0662-1>
- Scherliess L, Fejer BG (1999) Radar and satellite global equatorial F region vertical drift model. *J Geophys Res* 104(A4):6829–6842. <https://doi.org/10.1029/1999JA900025>
- Scherliess L, Thompson DC, Schunk RW (2009) Ionospheric dynamics and drivers obtained from a physics-based data assimilation model. *Radio Sci* 44:RS0A32. <https://doi.org/10.1029/2008RS004068>
- Schunk RW, Sojka LSJJ, Thompson DC, Anderson DN, Codrescu M, Minter C, Fuller-Rowell TJ, Heelis RA, Hairston M, Howe BM (2004) Global Assimilation of ionospheric measurements (GAIM). *Radio Sci* 39:RS1S02. <https://doi.org/10.1029/2002RS002794>
- Secan JA, Bussey RM, Fremouw EJ, Basu S (1995) An improved model of equatorial scintillation. *Radio Sci* 30(3):607–617. <https://doi.org/10.1029/94RS03172>
- Shuman FG (1989) History of numerical weather prediction at the National Meteorological Center. *Weather Forecast* 4:286–296. [https://doi.org/10.1175/1520-0434\(1989\)004%3c0286:HONWPA%3e2.0.CO;2](https://doi.org/10.1175/1520-0434(1989)004%3c0286:HONWPA%3e2.0.CO;2)
- Sun YY, Liu JY, Lin CY, Tsai HF, Chang LC, Chen CY, Chen CH (2016) Ionospheric F2 region perturbed by the 25 April 2015 Nepal earthquake. *J Geophys Res Space Phys* 121:5778–5784. <https://doi.org/10.1002/2015JA022280>
- Sun YY, Liu JY, Tsai HF, Krankowski A (2017) Global ionosphere map constructed by using total electron content from ground-based GNSS receiver and FORMOSAT-3/COSMIC GPS occultation experiment. *GPS Solut* 21:1583–1591. <https://doi.org/10.1007/s10291-017-0635-4>
- Syndergaard S (2006) COSMIC S4 Data, the First FORMOSAT-3/COSMIC Data Users Workshop in Boulder, CO, USA, October 16–18, 2006.
- Thaduri A, Galar D, Kumar U (2020) Space weather climate impacts on railway infrastructure. *Int J Syst Assur Eng Manag* 11:267–281. <https://doi.org/10.1007/s13198-020-01003-9>
- Torr MR, Torr DG (1973) The seasonal behaviour of the F2-layer of the ionosphere. *J Atmos Terr Phys* 35:2237–2257. [https://doi.org/10.1016/0021-9169\(73\)90140-2](https://doi.org/10.1016/0021-9169(73)90140-2)
- Torr DG, Torr MR, Richards PG (1980) Causes of the F region winter anomaly. *Geophys Res Lett* 7:301–304. <https://doi.org/10.1029/GL0071005p00301>
- Tsai HF, Liu JY, Lin CH, Hsu ML (2010) FORMOSAT-3/COSMIC observations of the ionospheric auroral oval development. *GPS Solut* 14(1):91–97. <https://doi.org/10.1007/s10291-009-0137-0>
- Tsai LC, Su SY, Liu CH et al (2018) Global morphology of ionospheric sporadic E layer from the For-moSat-3/COSMIC GPS radio occultation experiment. *GPS Solut* 22:118. <https://doi.org/10.1007/s10291-018-0782-2>
- Tulasi Ram S, Su S-Y, Liu CH (2009) FORMOSAT-3/COSMIC observations of seasonal and longitudinal variations of equatorial ionization anomaly and its interhemispheric asymmetry during the solar minimum period. *J Geophys Res* 114:A06311. <https://doi.org/10.1029/2008JA013880>
- Uma G, Liu JY, Chen SP, Sun YY, Brahmanandam PS, Lin CH (2012) A comparison of the equatorial spread F derived by the International Reference Ionosphere and the S4 index observed by FORMOSAT-3/COSMIC during the solar minimum period of 2007–2009. *Earth Planet Sp* 64:467–471. <https://doi.org/10.5047/eps.2011.10.014>
- Wang CY, Chu YH, Su CL, Kuong RM, Chen HC, Chu FD (2009) Campaign investigation of ionospheric plasma irregularities in sporadic E region using FORMOSAT-3/COSMIC satellite and Chung-Li 30 MHz coherent radar. *Terr Atmos Ocean Sci* 20:237–250. [https://doi.org/10.3319/TAO.2008.01.22.01\(F3C\)](https://doi.org/10.3319/TAO.2008.01.22.01(F3C))
- Yeh WH, Liu JY, Huang CY, Chen SP (2014) Explanation of the sporadic-E layer formation by comparing FORMOSAT-3/COSMIC data with meteor and wind shear information. *J Geophys Res Atmos* 119:4568–4579. <https://doi.org/10.1002/2013JD020798>
- Yeh WH, Lin CY, Liu JY, Chen SP, Hsiao TY, Huang CY (2020) Superposition property of the ionospheric scintillation S4 Index. *IEEE Geosci Rem Sens Lett* 17(4):597–600. <https://doi.org/10.1109/LGRS.2019.2928588>
- Yue X, Schreiner WS, Lei J, Rocken C, Hunt DC, Kuo Y-H, Wan W (2010) Global ionospheric response observed by COSMIC satellites during the January 2009 stratospheric sudden warming event. *J Geophys. Res.* 115:A00G09. <https://doi.org/10.1029/2010JA015466>

Publisher's Note

Springer Nature remains neutral with regard to jurisdictional claims in published maps and institutional affiliations.